SCANNING PROBE STUDIES OF THIN FILMS

Thesis by

Joseph Varghese

In Partial Fulfillment of the Requirements for the degree

of

Doctor of Philosophy

CALIFORNIA INSTITUTE OF TECHNOLOGY

Pasadena, California

2014

(Defended May 9, 2014)

Acknowledgements

I would first and foremost like to thank my advisor, Prof. James Heath, for giving me the opportunity to work in his research group. Thank you for giving me a chance to try my hand at science and advising my pursuits in a way that made me a far more independent researcher than I could have hoped to become on my own. I had a chance to work on cutting-edge research with several talented people and use amazing instruments that few other places in the world can boast about. Your intuition helped steer me clear of experimental pitfalls, while suggesting helpful alternatives that kept me engaged in projects that ultimately flourished.

I would like to extend my deepest thanks to Dr. Jamil Tahir-Kheli, who helped me in some of my most difficult times in my research – you exemplify what it means to be a kind genius. I worked with Peter Agbo, Ryan Henning, and Dr. Douglas Tham very closely on different projects, and I truly appreciate their constant support and true friendship. I greatly appreciate Dr. Peigen Cao, with whom I worked closely on the graphene-templating projects and who taught me a great deal about sample preparation and scanning probe techniques. I deeply thank Dr. Victor Brar for all his selfless help and advice, and for taking the time to help me with many difficulties in instrumentation and spectroscopy. I similarly thank Dr. Samir Das and Dr. Arundhati Nag for helping me learn synthetic chemistry techniques and for their sincere friendship and encouragement. I also thank Dr. Ke Xu, Dr. Jen-kan Yu, Dr. Slobodan Mitrovic, and Dr. Ruo-gu Huang for the chance to work with them on several projects.

thank my family – my father and mother, Philip and Susan Varghese, my brother, Philip

Varghese, and my sister, Merilyn Varghese. You have always loved me and supported me

no matter what – I love you so much – no son ever had better parents, and no brother ever

had better siblings. Lastly, I would like to thank Jesus Christ, who taught me to try to be a

moral person, and God for giving me life.

A b s t r a c t

The first part of this thesis deals with the phenomenon of thermoelectricity. It involves the improvement of the thermoelectric properties of silicon using innovative nanostructures. My contribution was to help fabricate these thermoelectric devices, and is the focus of this part of the thesis.

The second part and primary focus of this thesis is the analysis of thin films using scanning probe techniques. These surface techniques include atomic force microscopy, electric force microscopy, Kelvin probe force microscopy, and scanning tunneling microscopy. The thin films studied are graphene and molybdenum disulfide, two remarkable materials that display unique two-dimensional qualities. These materials are shown to be useful in studying the properties of adsorbates trapped between them and the substrate on which they rest. Moreover, these adsorbed species are seen to affect the structural and electronic properties of the thin films themselves. Scanning probe analyses are particularly useful in elucidating the properties of these materials, as surface effects play a significant role in determining their characteristics.

The final part of this thesis is concerned with the study of Akt in live cells using protein capture agents previously developed by my colleagues. The activation and degradation of Akt is investigated using various biological assays, including Western blots, in vitro kinase assays, and cell viability assays. Finally, the usefulness of synthetic capture agents in perturbing protein pathways and as delivery agents is assessed and analyzed.

Table of Contents

List of Figures

C h a p t e r 1

Nanostructured Silicon Thermoelectrics

1.1 Introduction

The field of thermoelectrics has been studied for well over a century, beginning with the discoveries of the Seebeck, Peltier, and Thomson effects in the 1800's. Since then, great advances have been made in developing thermoelectric materials and determining their properties. Many new and interesting phenomena have also been discovered, particularly in the area of nanostructures and devices. It is expected that these discoveries will aid in the development of efficient thermoelectric materials and further our understanding of thermoelectricity.

The great appeal of thermoelectric materials lies in their ability to convert a temperature difference into a voltage potential, and vice versa. Perhaps the primary usefulness of thermoelectrics lies in the ability to recover useful work from heat. Heat is often deemed an inevitable byproduct of a process, and is usually considered "useless" as compared to the work output. Thermoelectricity provides a way to render heat "useful" by converting temperature gradients generated by heat into electricity. It can thus be used to increase the overall efficiency of a process, even though it usually cannot replace the process itself. There are three primary thermoelectric effects: the Seebeck effect, the Peltier effect, and the Thomson effect.

In the Seebeck effect, a current is generated in response to an imposed temperature gradient. This current can be readily observed in a simple circuit composed of junctions between dissimilar metals (labeled A and B), as displayed in Figure 1. If the metals were of the same type, the Seebeck effect would not be observed, since the circuit would be symmetric.[1] Prior to the imposition of a temperature gradient, the system is in a state of equilibrium. The heating up of one junction causes carriers to move to the other in an attempt to restore equilibrium. The movement of these carriers generates a current which then flows through the circuit.[2] A potential difference is thus created that can be measured or used to do work. The ratio of the voltage potential to the difference in temperature is called the thermopower, or S.[1] The Seebeck effect can also be observed in semiconductors. The circuit diagram is displayed in Figure 1. In this case, two metals are joined by n-type and p-type materials. When heat is applied to one side, both electrons and holes in the respective materials will move in the same downward direction and cause a current to flow through the circuit.[3]

In the Peltier effect, heating or cooling occurs at junctions of two dissimilar metals (labeled A and B) in response to an imposed current. It is thus commonly called "the opposite of the Seebeck effect", and is depicted in Figure 2. Because the two materials have different entropies of transport, an incomplete transfer of energy occurs between the electrons flowing through one metal and those flowing in the other. Thus, one junction must heat up and the other must cool down in order to conserve energy.[2] A similar situation occurs for semiconductors, as shown in Figure 3. If the two metals are joined by n-type and p-type materials, the electrons and holes will move downward, respectively, when a voltage

potential is applied. As before, one junction will heat up while the other cools down in order to conserve energy.[3]

The Thomson effect occurs when both a temperature gradient and a voltage potential are applied to a material (labeled A), as in Figure 4. In this case, heat is absorbed or emitted from the material along its entire length. This is because the varying temperature causes the Seebeck coefficient – which depends on temperature – to vary along the length of the material. This causes a differential Peltier effect to occur, resulting in the observed heating or cooling.[2] The absorption or emission of heat also depends on the direction of current. If a material is initially absorbing heat as a result of the Thomson effect, a reversal of current will cause the material to emit heat instead (see Figure 5).[1]

The Seebeck, Peltier, and Thomson effects all provide ways in which to harness and convert energy into useful forms. Unfortunately, the thermoelectric materials that exhibit these effects are limited in their usefulness due to their poor efficiency. To determine whether a material is thermoelectrically efficient, it is necessary to evaluate its figure of merit. The figure of merit is given by: $Z = S^2 \sigma T / \kappa$.[4] By examining the figure of merit, it is easily seen that three of its components (without considering the temperature) can be altered to yield higher values. These are the thermopower, the electrical conductivity (σ), and the thermal conductivity (κ). It is obvious that large values of the thermopower and electrical conductivity, and small values of the thermal conductivity, are desirable. Since the figure of merit depends on the square of the thermopower, an increase in this quantity can greatly improve the value of the figure of merit.

The difficulty in altering one component is that it often adversely affects the others. For example, in metals, the thermal and electrical conductivities are strongly coupled and

an increase in one almost always results in an increase in the other. This is because both heat and electricity flow well in metals due to the large number of carriers. The situation is further complicated by the fact that the Seebeck coefficient will also vary with the carrier concentration.[5]

Yet another difficulty encountered is that the thermopower, electrical conductivity, and thermal conductivity all depend on temperature. Thus, simply increasing the temperature will not assuredly increase the value of the figure of merit. The effects of increasing or decreasing the temperature are difficult to predict, and are specific to the system or material of interest.

Fortunately, many of these problems become much easier to deal with by using semiconductors. For example, the thermal and electrical conductivities are not as strongly coupled as in metals. The electrical and thermal properties of semiconductors can also be more readily altered – particularly through processes such as doping. For example, through doping one can alter the number and type of carriers in a semiconductor. This is important, because both the electrical conductivity and the electronic thermal conductivity depend directly on the carrier concentration.[5] Furthermore, by using semiconductors of high atomic weight, one can decrease the speed of sound in a material and thereby lower the thermal conductivity.[4] The lattice thermal conductivity (the other constituent part of the thermal conductivity) is predominantly governed by the phononics of the system, and can also be altered by changing the size and shape of the semiconductor.[4,5] Thus, by using semiconductors, one can influence thermoelectric behavior in such a way as to produce efficient materials for scientific applications.

The potential applications of thermoelectricity are many, some of which are in use today. Among these are thermocouples, which use the Seebeck effect in order to gauge temperature differences. Thermocouples consist of a circuit made of two dissimilar metals connected to a voltmeter. When a temperature gradient exists across the junctions of the metals, a voltage is generated that can be used to measure the temperature difference. Apart from their use in laboratories, thermocouples are well-known for having been used in NASA's Radioisotope Thermoelectric Generators, or RTGs. Heat is produced by a radioisotope such as Pu-238, which thermocouples then convert into electricity.[6]

Currently, thermoelectric materials are too inefficient to be used for a variety of purposes. The simplest ways to overcome this are to discover new materials, or to fine-tune the properties of already existing ones. One of the most effective ways to accomplish the latter is by exploiting structural characteristics at the nanoscale.

The overall process begins with the fabrication of the nanomesh from two sets of nanowires. Much of the processing techniques and analysis of the nanomesh structures are based on a similar investigation of SNAP nanowires performed by Boukai *et.al.*[8] This is done using SNAP, or superlattice nanowire pattern transfer. It involves the use of $GaAs/Al_{0.8}Ga_{0.2}As$ superlattices in order to produce ultrahigh density arrays of nanowires using a one-step deposition process.[7] The superlattices are first etched, and platinum is deposited in the gaps. The superlattices are then placed on top of a silicon substrate, and are held in place with epoxy. Both the superlattice and the substrate are then placed in an etching solution. When sufficient time has passed, the superlattice is removed, leaving an imprint of platinum nanowires. The pattern can then be transferred to silicon via a vapor etch. The process is depicted in Figure 6.

Using this method, parallel sets of nanowires up to 400 in number can be made. The pitch (center-to-center distance) is usually around 30 nm, and the diameter around 10-20 nm. Both the pitch and the diameter of the wires can be changed by using a different SNAP master. When the SNAP procedure is repeated twice, with the etching step omitted on the first SNAP run, a nanomesh is made. On the second SNAP run, a SNAP aligner is used to place the second superlattice on top of the imprint left by the first one. In this case, the imprint consists of the platinum nanowires, since the vapor etch transfer to silicon can only be done once the second superlattice is in position. The placement of the second superlattice can be done at an angle if desired, but only perpendicular placements have been carried out so far. The area of intersection of the two sets of nanowires is typically around 10 μm x 10 μm. A typical SNAP nanomesh that I made using this procedure (formed of platinum wires – etching into silicon still to be done) is shown in Figure 7.

When the platinum nanomesh is made, the entire pattern can be transferred to silicon using a CF_4 vapor etch. Once the silicon nanomesh is made, a device platform consisting of two heaters and four electrodes is used to perform measurements of the various components of the figure of merit. In addition, the platform is made in such a way so as to allow suspension of the nanomesh structure.

Suspending the nanomesh is not a trivial task, as the residual stresses in the substrate greatly contribute to the breaking of the fine structure. The device fabrication method we used is outlined below.

1.2 Experimental Methods

All devices were prepared on silicon-on-insulator (SOI; Soitec Inc.) wafers. The

SOI wafers were pre-doped by thermally diffusing spin-on-dopant (Boron A; Filmtronics, Inc.) with rapid thermal annealing (RTA) at 820°C for 3 minutes. The resulting sheet resistance indicates a doping concentration of $2\text{x}10^{19}$ cm^{-3}, with the thickness of the silicon epilayer determined by atomic force microscopy to be 25 nm, 22 nm, and 20 nm (depending on the device) with a variance of 1 nm. The nanomesh films (NM) and nanowires (NWA) are fabricated by the SNAP technique, while the e-beam nanomesh (EBL NM) and thin films (TF) are defined by e-beam lithography (EBL).

For the NM devices, two orthogonally aligned Pt nanowire arrays, or Pt cross-bars, are made using two consecutive SNAP procedures on top of an SOI wafer (Soitec, Inc.) with the pitch and width of the Pt nanowires pre-determined by the superlattices. In contrast, for the NWA devices only one SNAP procedure is carried out, resulting in one Pt nanowire array. For the EBL NM and TF devices, e-beam lithography and metallization are used to make the transfer-ready Pt nanostructures. Next, we define the membranes and the beams (hereafter referred to as device platform) by electron-beam lithography (EBL) and electron-beam assisted metal evaporation. The pattern transfer is performed by CF$_4$/He reactive ion etch (hereafter referred to as RIE1). The etch is terminated at the buried oxide layer by endpoint detection via surface reflectivity measurement. Afterwards, Pt is removed by aqua regia (HNO$_3$:HCl = 1:3), followed by 10 minutes of piranha (H$_2$SO$_4$:H$_2$O$_2$ = 5:1) cleaning. At this point, both a silicon device (NM, EBL-NM, NWA or TF) and a silicon device platform have been made (Figure 8a). The following steps are identical regardless of the device type.

An Al etch mask is placed on top of the device to protect it in subsequent

fabrication steps. The top few nanometers of the device platform are removed at this

point by RIE1 to make it electrically insulating. A 250 nm-thick low-stress silicon-nitride

film, which serves as a structural backbone to the platform, is then deposited via plasma

enhanced chemical vapor deposition (PECVD, STS Multiplex). Another Al etch mask is

then placed on top of the silicon-nitride layer, and patterned to match the device platform.

Subsequent RIE1 process therefore defines the silicon-nitride film to match the shape of the

platform and removes it elsewhere. Al is then removed using an acidic mixture

(H_3PO_4:CH_3COOH:HNO_3:H_2O = 16:1:1:2). The resulting structure looks much the same

as before, but has been greatly strengthened by silicon-nitride (Figure 8b). Next, the

platinum resistive thermometers (PRT), which also serve as heaters, are fabricated by EBL

and metallization – typically, 60 nm of Pt is deposited on top of a 10 nm Ti adhesion layer

(Figure 8c).

Device suspension involves gas phase mechanisms: XeF_2 and HF vapor. It is

necessary to protect the device platform from potential damage by the HF vapor, and this is

done by depositing a layer of poly(monochloro-*p*-xylylene) or parylene-C (200 nm-thin

film; SCS parylene deposition system). Prior to parylene coating, an Al metal mask was

deposited onto the device to prevent direct contact with parylene. Similarly, another metal

etch-mask, Al or NiCr, is placed on top of the parylene layer and over the device platform.

O_2 plasma is then used to etch through parylene, and results in a structure that is now

protected from HF vapor damage (Figure 8d). It is necessary to also etch through the buried

oxide layer and reach the underlying silicon substrate. This is to facilitate the removal of

the buried oxide under the device in order to achieve a fully suspended device. RIE1 etch is

again used to etch through the oxide, stopping once the silicon layer has been reached

(Figure 8e). As before, an Al film was protecting the device including the platform from etching. After the removal of Al, the device and the platform are ready for suspension.

A layer of 6% polymethyl methacrylate (PMMA) e-beam resist is spun on the chip, and two openings in PMMA are patterened on each side of the device platform. XeF_2 etch (custom XeF_2 pulsed etching system) through the holes is isotropic and undercuts the device platform, releasing it from the chip (Figure 8f). The overall etch time is about 2 minutes at 2000 mTorr and room temperature. The PMMA layer is then removed using an acetone bath, followed by methanol, before finally drying by a CO_2 supercritical drying process (Automegasamdri-915B, Tousimis).

An HF vapor etch process is now applied to release the device from the buried oxide substrate, resulting in a fully suspended device (Figure 8g). A home-built HF vapor etcher equipped with a wafer heating stage was designed for homogeneous and stiction-free oxide removal at elevated temperatures. The etching process is performed with the wafer heated at a temperature of ~80°C and exposed to HF environment for ~30 minutes to completely remove the buried oxide layer of ~125 nm in thickness. The sample is wire-bonded to a chip that is promptly inserted into a vacuum measurement system. The suspension procedure was ultimately successful in allowing the isolation of the nanomesh structure and the investigation of its thermoelectric properties. It was found that the thermal conductivity of the nanomesh was indeed decreased compared to its bulk counterpart.[9] By changing the physical characteristics of the nanomeshes, it is expected that the optimal setup to maximize the figure of merit can be achieved. These physical parameters include the pitch and diameters of the nanowires, and the angle at which the SNAP nanowires are

placed on top of each other. Moreover, the placement of the heaters can be varied – for

example, placing them at right angles to each other will force a phonon to make a ninety

degree bend in order to reach the other side. A highly-simplified theoretical analysis of this

situation is presented in the following section.

One method by which we originally proposed to decrease the thermal conductivity

of the SNAP nanomesh is by placing the heaters at right angles to one another. When this

happens, the phonons propagating through the structure will have to "bend" around a

corner in order to reach the other end of the nanostructure. It is expected that a significant

portion of the phonons will be reflected when this occurs.

1.3 Phononic Model

In order to demonstrate this theoretically, Dr. Jamil Tahir-Kheli of the Goddard

Group and I developed a model that, though very simple, elucidates some of the essential

physics of the argument. I then solved the relevant differential equations involved, and used

MATLAB to depict the results graphically. In order to model the bend that a phonon would

encounter, we used a chain of particles connected to each other by springs. The particles

had identical masses, but the spring constants of the springs placed in-between them were

different, as displayed in Figure 9.

Thus, two chains of particles, each connected to infinite half-chains, were joined

together by a corner atom. I unfolded the two-dimensional system into a one-dimensional

system, the difference in the spring constants K and G providing a way to effectively depict

the "bend". Since the spring constants are different, reflection and transmission of a phonon

mode will occur, portraying the occurrence of a phonon entering a bend. For the bottom

chain, the wavefunction can be written as: $\psi_1 = (e^{ikna} + Re^{-ikna}) e^{-iwt}$, where R is the reflection coefficient, and for the top chain, the wavefunction can be written as: $\psi_2 = Te^{i(kna-wt)}$, where T is the transmission coefficient. Plotting the reflection and transmission coefficients for varying wavenumber yields physical information as to the degree to which a phonon will pass through the bend. Since the wavenumber is inversely proportional to the wavelength, it is predicted that the effect of the bend will be increasingly important at higher frequencies.

The model was solved by using a system of linear differential equations which, when diagonalized in a matrix representation, yielded the desired coefficients. The square of the modulus of the coefficients was then plotted, a typical plot being depicted in Figure 10. In this particular case, the spring constants were all different, except for the symmetric springs I and J. It can be seen that the reflection coefficient increases as the wavenumber increases, while the transmission coefficient decreases.

As the wavelength decreases, the phonon is more likely to "notice" impurities or defects in a lattice, or in this case, the "bend" in the structure. At long wavelengths, the phonon tends to "glide" over these defects or irregularities, and can still propagate quite efficiently. Thus, for large wavelengths or small wavenumbers, the phonon will be transmitted rather than reflected. At much shorter wavelengths, the opposite is true. This physical reasoning corresponds well with the results of the model. For large values of the wavenumber, the reflection coefficient is large, while the transmission coefficient is low. Thus, in this specific model, the short wavelength phonons are likely to be reflected when they encounter the bend.

It must be noted that the model is highly simplified and does not depict the actual structure in a very realistic manner. For example, only longitudinal displacements are allowed, only one chain of atoms is used, and interactions are almost all nearest-neighbor couplings. Thus, the usefulness of the model lies primarily in its very simple demonstration of a physical concept, but perhaps not in its predictive ability. It also provides an intuitive grasp of the physical reasoning for placing the thermoelectric heaters at angles to one another.

1.4 Figures
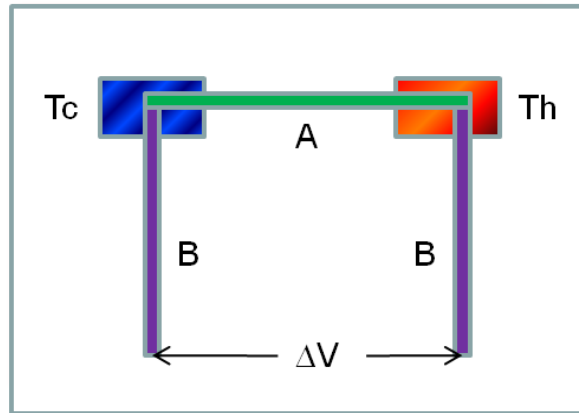
Figure 1 - Seebeck Effect
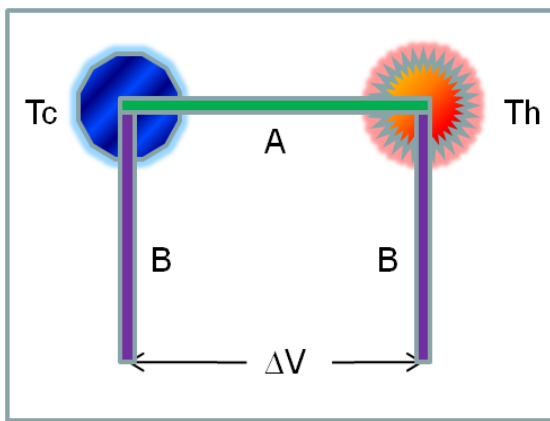
Figure 2 - Peltier Effect
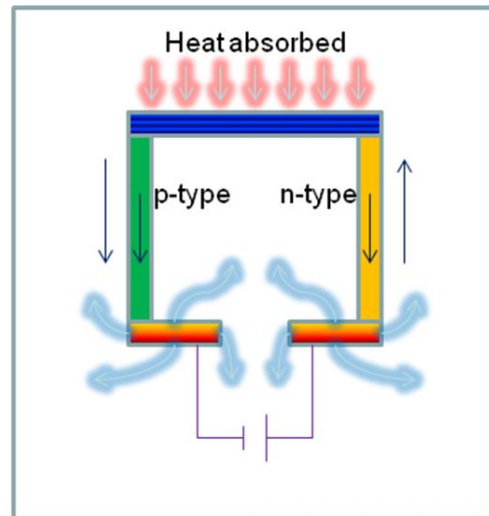
Figure 3 - Peltier Effect
(Semiconductors)
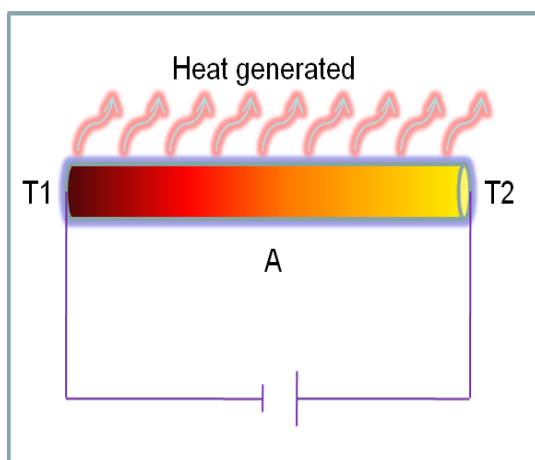
Figure 4 - Thomson Effect
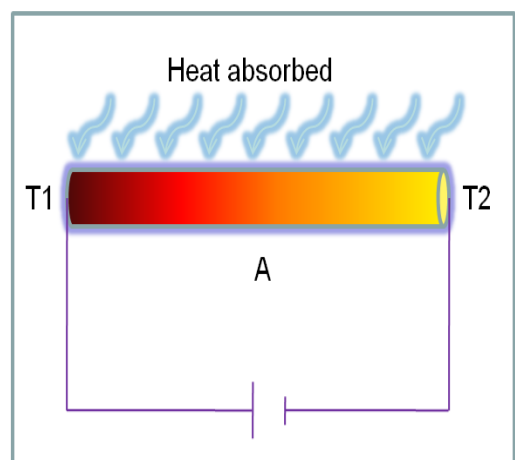
Figure 5 - Thomson Effect (Current Reversed)
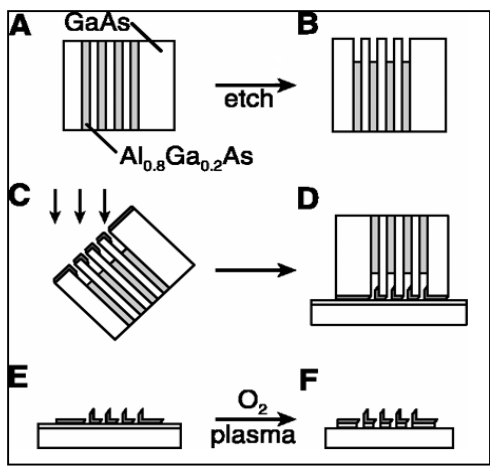
Figure 6 - SNAP Process[7]
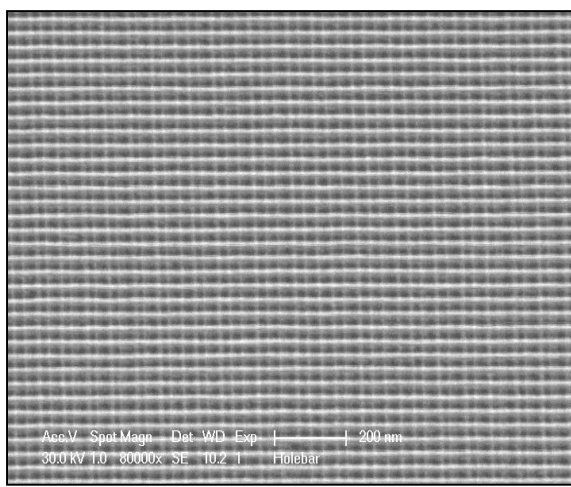
Figure 7 – Platinum Nanomesh
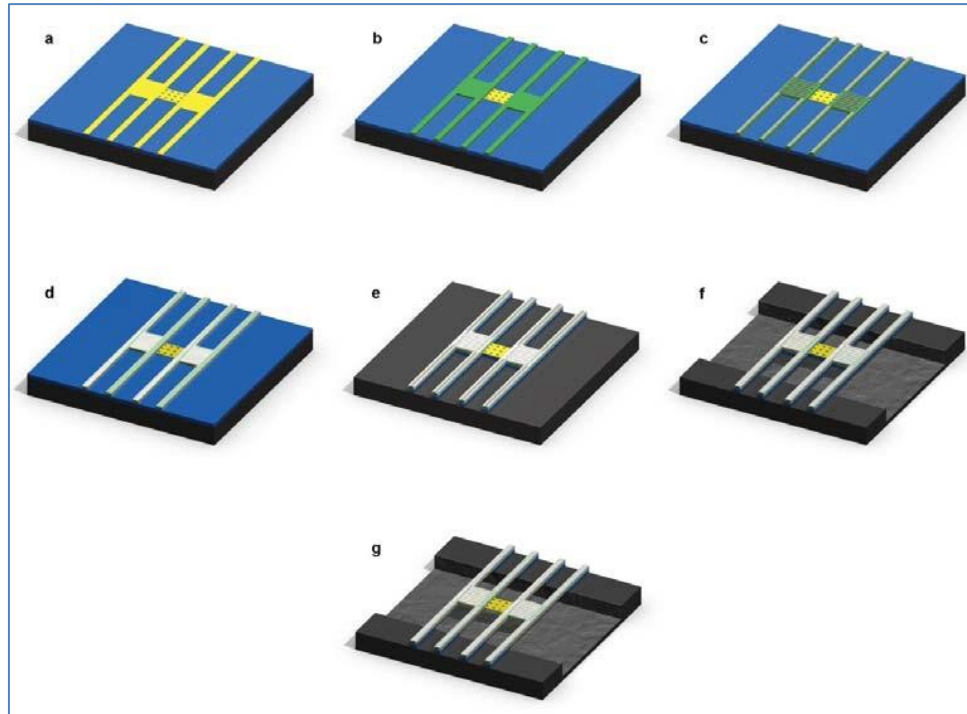
Figure 8 – Device fabrication. The scale of the device is exaggerated from reality for better visualization. (a) Silicon nanomesh with monolithically-defined silicon device platform. (Yellow). (b) Device platform with silicon-nitride film as the structural backbone. (c) Ti/Pt heater/sensor defined on to the platform. (d) Parylene C conformally deposited on to the platform. (e) Buried oxide removed by RIE1 process. (f) Si handle layer etched by XeF2. (g) Device fully suspended by buried oxide removal with HF vapor.
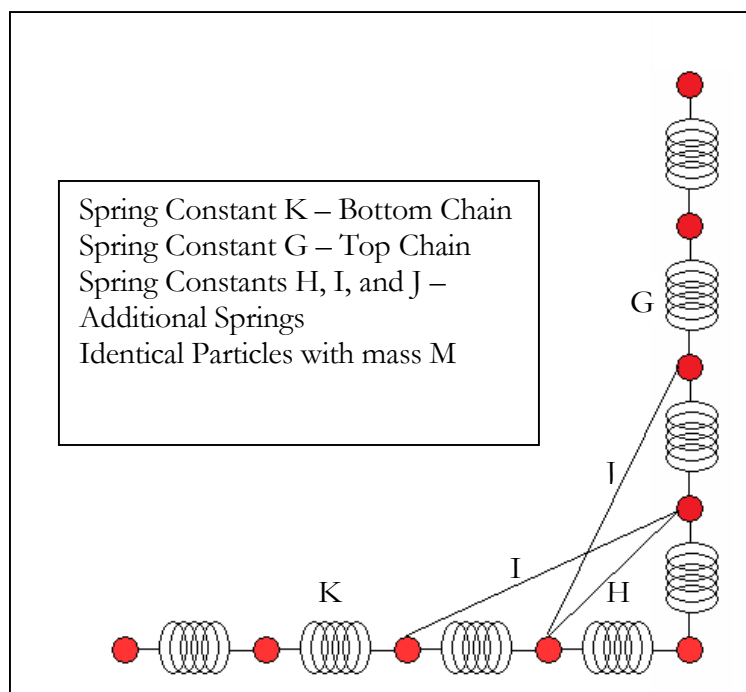
Figure 9 – Simplified Nanomesh Model
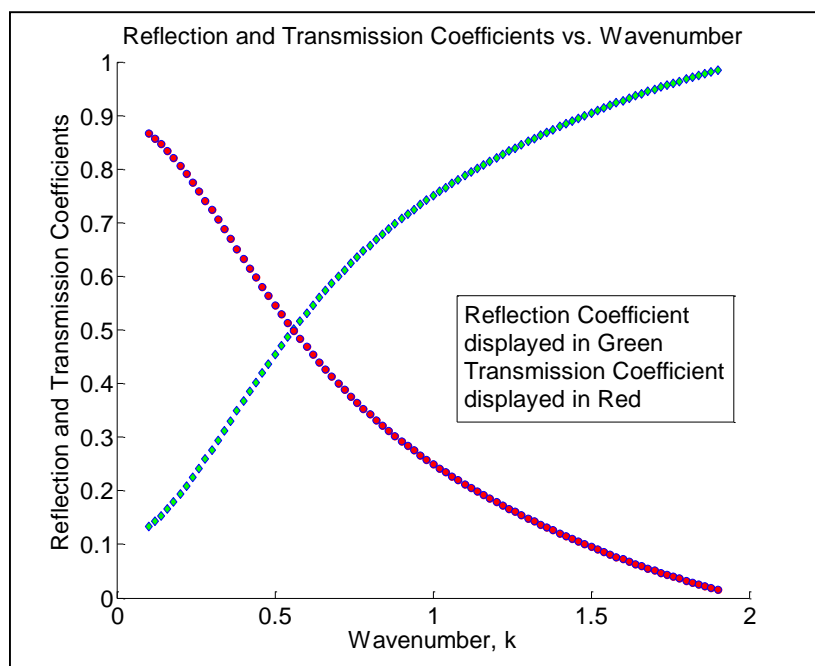
Figure 10 - Coefficients R and T vs. Wavenumber

1.5 References

1.   MacDonald, D. <u>Thermoelectricity: An introduction to the principles</u>. New York: John Wiley & Sons, Inc., 1962. 2,5,7,14, 89.

2.   Teutsch, W. "Some Considerations of the Basic Physics of Thermoelectric Effects," <u>Thermoelectricity</u>. Ed. Paul Egli. New York: John Wiley & Sons, Inc., 1960. 27.

3.   Ramberg, E.; Rosi, R. "Evaluation and Properties of Materials for Thermoelectric Applications," <u>Thermoelectricity</u>. Ed. Paul Egli. New York: John Wiley & Sons, Inc., 1960. 122.

4.   Majumdar, A. *Thermoelectricity in Semiconductor Nanostructures,* Science, 2004. **303:**777-778.

5.   Heikes, R.R.; R.W. Ure, Jr. "Introduction," <u>Thermoelectricity: Science and Engineering</u>. Robert Heikes and Roland W. Ure, Jr. New York: Interscience Publishers, 1961. 19.

6.   Rinehart, G. *Design characteristics and fabrication of Radioisotope Heat Sources for Space Missions,* Progress in Nuclear Energy, 2001. **39**:305-319.

7.   Melosh, N. *et. al., Ultrahigh-Density Nanowire Lattices and Circuits,* Science, 2003. **300:**112-115.

8.   Boukai, A. *et. al., Silicon Nanowires as Efficient Thermoelectric Materials,* Nature, 2008. **451:**168-171.

9.   Yu, J.K. *et. al., Reduction of thermal conductivity in phononic nanomesh structures,* Nature Nanotech., 2010. **5:** 718-721.

C h a p t e r   2

Graphene-templating of Organic Molecules

2.1 Introduction

In a previous study by co-authors Ke Xu and Peigen Cao, the graphene templating technique was employed to probe the structure of water adlayers on mica under ambient conditions.[14] The technique involved the exfoliation of graphene onto mica substrates, and the water layers trapped between the graphene and substrate were characterized. We determined that substances other than water could be templated with graphene through proper sample preparation, and decided to investigate organic molecules.

The first layers of organic molecules adsorbed to solid surfaces often determine the physics and chemistry of both the adsorbate and the substrate, and thus play a crucial role in many applications, including, for example, heterogeneous catalysis, corrosion, adhesion, lubrication, and environmental control.[1-3] However, the structures of adlayers at the interfaces between solids and *vapors* of small organic molecules are poorly understood at room temperatures. The reasons are twofold. First, organic compounds capable of forming vapors at room temperatures are inevitably volatile, and so molecularly thin adlayers on surfaces quickly evaporate away in the vacuum environments required by many surface characterization techniques. Second, when vacuum is not required, the microscopic structure of the adlayers is still difficult to probe due to the mobile nature of small

molecules on surfaces, although certain area- and time-averaged properties can be determined (e.g., the averaged thickness of adlayers[4]).

As a result of these difficulties, previous experimental work on the room-temperature structures of organic molecule adlayers (or molecularly thin films) on solids has largely been limited to nonvolatile molecules (boiling point >>~250 °C) with high molecular weighs (number of carbon atoms >>10).[5-11] Such adlayers (thin films) are typically obtained through coating from a solution phase, and so are fundamentally different from adlayers in equilibrium with a vapor. Alternatively, adlayers of small organic molecules have been studied at low temperatures (T<<200 K), where the vapor pressure and mobility of molecules are drastically reduced.[1,3,12,13] However, the adlayer structures are found to be highly temperature-dependent,[3,12] and thus the low-T results cannot be directly compared with the room-temperature vapor adsorption one encounters in everyday life.

We use graphene sheets as an ultra-thin coating/template for the atomic force microscopy (AFM) characterization of the room-temperature structures of the adlayers at the interfaces between mica surfaces and vapors of small organic molecules. In the current work, we show that graphene, albeit only one-atom thick, can prevent the evaporation of molecularly thin adlayers of volatile small organic molecules, and slows down the motions of the molecules on the solid surface, thus allowing AFM observation of both the *structure* and *dynamics* of the adlayers at room temperature. Two common small organic molecules, tetrahydrofuran (THF) and cyclohexane, each representing one of the two classes of polar and non-polar organic solvents, were investigated and compared with water.

2.2 Experimental Methods

Materials: Anhydrous inhibitor-free tetrahydrofuran (THF, ≥99.9%, water content <0.002%) and anhydrous cyclohexane (99.5%, water content <0.001%) were purchased from Sigma-Aldrich. These reagents were used as supplied and stored in a glove-box purged with nitrogen. Muscovite mica (Grade V1; round disks of diameter 10 mm) was obtained from Ted Pella. Kish graphite was obtained from Covalent Materials US Inc.

Sample preparation: Samples were prepared in a glove-bag (Sigma-Aldrich AtmosBag) that was purged and protected under a continuous flow of ultra-high purity argon, in which the relative humidity (RH) was controlled to be <2%. Humidity was monitored using a Fluke 971 temperature humidity meter. All experiments were performed at room temperature (22±2 °C). Mica disks were first heated in air at 200 °C for 10 min to remove absorbed moisture, and then transferred into the glove-bag. The mica surface was cleaved in the glove-bag and exposed to organic vapors for ~10 s to ~1 min. The partial pressure of organic molecules at the mica surface, which determines the surface coverage at equilibrium, was adjusted by varying the distance between the vapor source and the mica surface. Graphene sheets were deposited onto the mica surface through the standard method of mechanical exfoliation of Kish graphite, thus sealing and preserving the adlayers of organic molecules.

Mechanical exfoliation: A few pieces of Kish graphite flakes were first placed on a piece of Scotch-tape that was repeatedly closed on itself and then re-opened. This process caused the tape to be covered with many flakes of graphite of varying thicknesses. The tape was then carefully set aside until the substrates were ready for deposition of the graphene layers.

Identification of graphene layers: Monolayer graphene sheets were identified through optical microscopy and confirmed by spatially resolved Raman (Fig. 4). Raman spectra were recorded with a Renishaw M1000 Micro Raman spectrometer system using a 514.5 nm laser beam and a 2400 lines per mm grating. A confocal optical microscope with a 100x objective lens was used to record spectra with a spatial resolution of 2 μm. No noticeable D peak was observed in the Raman spectra, indicating high-crystalline order of our samples.

Atomic Force Microscopy: All AFM images were acquired under tapping mode on a Digital Instrument Nanoscope IIIA at ambient conditions. A sharp TESP tip (Veeco) with a radius of end of 8 nm was used. Typical values for the force constant and resonance frequency were 42 N/m and 320 kHz respectively. Height calibrations were performed using the step heights of freshly cleaved graphite samples. Due to the super-flatness of the samples, sometimes the laser interference pattern along the slow-scan axis was hard to avoid, which is more noticeable in large-area scanning and has a period of twice the wavelength of the laser. This is caused by the constructive interference of laser reflected from the sample surface with that reflected from the cantilever. The broad stripe-like features seen in Fig. 1a were due to this effect.

2.3 Results and Discussion

Figs. 1b-f present typical AFM images of monolayer (as confirmed by Raman spectroscopy) graphene sheets deposited on mica surfaces that were in equilibrium with THF vapors, obtained within a few hours after sample preparation. Atomically flat islands/plateaus are observed across all graphene sheets. In comparison, no island-like

structures are observed on mica surfaces that are not covered by graphene. Phase images indicate that the observed flat islands are THF adlayers trapped under the graphene sheets, similar to the case of water adlayers.[14] The numbers of THF adlayers, as labeled in Fig. 1, were determined from measured heights and careful tracing of the extreme edges of graphene sheets, where the adlayers under graphene tend to evaporate away and leave the graphene in direct contact with the bare mica surface.[14]

Fig. 1b-d present the case in which the trapped adlayer is a submonolayer. Large, interconnecting islands are observed to coexist with areas where no adlayer is present. At low surface coverage, the adlayers tend to form narrow "necks" as opposed to isolated small islands (Fig. 1d). This result is very different from submonolayers of water adlayers at low coverage, where isolated and scattered small islands, typically ~10 nm in lateral size, are observed.[14] This result suggests that when compared to water, THF molecules interact more weakly with the inorganic mica substrate, so the interactions between THF molecules dominate and lead to more continuous adlayers.

The boundaries of the islands formed by the first THF adlayers often appear rounded (Fig. 1b-d). Similar rounded boundaries are also observed at the missing edges of full monolayers. These results suggest that the first THF adlayer is liquid-like. The second adlayers (Fig. 1e), on the other hand, exhibit both rounded and faceted boundaries. As will be discussed further, we also found that the boundaries of THF adlayers gradually become more faceted over time scales of weeks, suggesting that the adlayers possess both liquid and solid properties at room temperature. These results also contrast with water, for which both the first and second adlayers appear ice-like at room temperature, and are characterized by faceted boundaries with preferred angles of ~120°.[14-16]

The heights of the first and second THF adlayers on the mica surface, across ~10 different samples, were measured to be 0.42±0.02 and 0.44±0.02 nm, respectively (95% confidence interval). The height of the second adlayer is in good agreement with the layer thickness in THF crystals: THF crystallizes in the monoclinic space group $C2/c$, and the layer thickness in the b direction is $b/2$~0.447 nm.[17-19] In this direction, THF molecules "stand up" with the oxygen atoms in the rings alternatively pointing towards and away from the substrate,[19] which is plausible since this is also the polarity direction for THF molecules. The height of the first adlayer is found to be statistically thinner than the second adlayer; when the uncertainty in height calibration is ignored, the heights of the first and second THF adlayers can be expressed as 0.423±0.008 and 0.444±0.012 nm, respectively. This result suggests the first THF adlayer may be slightly thinner than the layer thickness in crystal. One possible explanation is that the molecules in the first adlayers are slightly tilted due to interactions with the substrate, a phenomenon often encountered in self-assembled monolayers on substrates.[20]

Fig. 2 presents typical AFM images of monolayer graphene deposited on mica surfaces that were in equilibrium with cyclohexane vapors at room temperature. Atomically flat islands are again observed for cyclohexane adlayers trapped under graphene. Similar to the case of THF but different from water, cyclohexane adlayers form large, continuous islands on the mica surface, indicative of weak molecule-substrate interactions. On the other hand, similar to the case of water but different from THF, the boundaries of all cyclohexane adlayers appear faceted, suggesting the adlayers are crystal-like solids. Although the non-polar cyclohexane molecules are expected to interact more weakly with the mica surface when compared to the polar THF molecules, the first adlayer of

cyclohexane on mica appears crystallized at room temperature, while the first adlayer of

THF appears liquid-like. This is likely due to the large difference in melting points.

Cyclohexane has a melting point of 6.7 °C, which is close to room temperature and much

higher than that of THF (−108.4 °C). Therefore, the crystal-like structures observed for the

room-temperature adlayers of cyclohexane and water are likely due to the combined effects

of relatively high melting points of the molecules and the geometric confinements of

molecules on the surface (restriction of motion in two dimensions). Second adlayers of

cyclohexane are only occasionally observed (Fig. 2b), typically surrounding droplets that

are likely attracted by surface defects.

The heights of the first and second cyclohexane adlayers on the mica surface across

different samples are measured to be 0.48±0.02 and 0.50±0.02 nm, respectively. These

values are in good agreement with the layer thickness of Phase I of crystal cyclohexane.

Phase I is the stable phase for bulk cyclohexane between 279.8 K and 186 K. The unit cell

is face-center cubic (fcc) with $a = 0.861$ nm.[21,22] The layer thickness in the (111) direction

(i.e., a close-packed hexagonal single layer) is thus $a/\sqrt{3} \sim 0.497$ nm. Previous low-energy

electron diffraction (LEED) studies[12,13] over large areas of cyclohexane adlayers on Pt(111)

and Ag(111) surfaces indicated that for $T < \sim 200$ K, cyclohexane adsorbs as a monoclinic

phase, which is consistent with the Phase II of crystal cyclohexane known to be stable for T

< 186 K in bulk. According to this arrangement, the cyclohexane rings would lie roughly

parallel to the substrate,[12,13] and the layer thickness should be $\sim c/2 \sin\beta = 0.407$ nm.[21] This

value is significantly smaller than the 0.48±0.02 and 0.50±0.02 nm adlayer heights we

measured. No LEED patterns were observed in previous studies for $T > \sim 200$ K, where

cyclohexane adlayers start to evaporate away in vacuum.[12,13] Our results suggest that at

room temperature, cyclohexane adlayers crystallize as Phase I that is stable between 279.8 K and 186 K in bulk. Phase I of cyclohexane is plastic crystal, meaning that although molecules form ordered crystal lattices, they are still free to rotate about the lattice points.[21,22] The layer height is thus larger than the case of Phase II, in which all molecules lie "flat" on the substrate.

Similar to the case of THF, the height of the first adlayer of cyclohexane is statistically thinner than the second adlayer: discounting the uncertainty in height calibration, the heights of the first and second cyclohexane adlayers are 0.480 ± 0.008 and 0.503 ± 0.012 nm, respectively. The height of the first adlayer may thus be slightly smaller than the layer thickness in the plastic crystal structure. Interactions with the substrate may restrain the rotation of cyclohexane molecules on the mica surface; the layer height is thus slightly smaller.

We further show that the graphene coating slows down the motion of adsorbed molecules, thus enabling the AFM observation of the dynamics of highly mobile adlayers. Under ambient conditions the graphene-templated cyclohexane adlayers are stable for months without noticeable changes in structures. Similar results were observed for water adlayers[14]. For water, graphene-templated adlayers are also stable for months under ambient conditions, and noticeable structural changes only occur at $T >\sim70$ °C. Both cyclohexane and water adlayers appear solid-like at room temperature, and so relatively low motilities can be expected.

Significantly different results are observed for THF adlayers. Although the graphene-templated THF adlayers are found to be stable over time scales of hours (e.g., the same structures are observed for images taken at different magnifications over periods of

several hours), noticeable structural changes are observed over time scales of weeks. In most cases, the adlayers shrink in lateral dimensions to form large droplets (Fig. 3b-d, in comparison with Fig 1c,e,f,). Narrow "necks" in the adlayers thus tend to break (blue arrow in Fig. 3b). We also note that the boundaries of the THF adlayers often become more faceted during the reorganization (Fig. 3b-d). These observations are reminiscent of the coalescence of molecularly thin clusters/islands often encountered during the post-deposition relaxation processes in thin film deposition.[23-25] In our case, adlayers are sealed under graphene, so the vapor-adlayer equilibrium is removed for the otherwise volatile molecules. The adlayers thus relax in a manner that is similar to deposited nonvolatile thin films. We further note that after the adlayers are allowed to relax for sufficiently long periods (Fig. 3ef), reverse processes, in which droplets shrink in size to form larger adlayer islands, are also occasionally observed (Fig. 3g). Such reversible island-droplet-island transitions are likely due to thermal fluctuations.

The observations that the THF adlayers often initially have round boundaries and are much more mobile than cyclohexane and water adlayers suggest that the adlayer is liquid-like. On the other hand, the observed reorganization of adlayers into faceted structures suggests the adlayers still possess some crystallinity at room temperature. This is quite remarkable, as room temperature is ~130 K higher than the bulk melting point of THF (−108.4 °C). The coexistence of solid-like and liquid-like layers have recently been observed for the ionic liquid Bmim-PF$_6$ on mica surfaces.[26] However, the melting point of Bmim-PF$_6$ (6.6 °C) is close to room temperature, and the liquid-like and solid-like structures observed in films of unknown thicknesses[26] likely only reflect the differences between bulk and adlayer properties. The faceted yet mobile adlayers we observed have not

been reported before. One possible explanation of our result is that the THF adlayers are in a "hexatic" phase that is between the solid and liquid phases; whereas in three dimensions liquid-solid transitions are necessarily first-ordered, for two-dimensional systems the liquid-solid transition may occur continuously through the intermediate "hexatic" phase over a wide temperature range.[27-29]

2.4 Conclusions

In summary, we have reported on the room-temperature structures and dynamics of weakly bound adlayers at the interfaces between solids and vapors of small organic molecules by using graphene templating. We found cyclohexane adlayers on mica appear crystal-like at room temperature, whereas THF adlayers possess both liquid and solid properties. The heights of the second adlayers of THF and cyclohexane are in good agreement with the layer thicknesses in the monoclinic crystal structure of THF and the Phase I "plastic crystal" structure of cyclohexane, respectively. The first adlayers of both molecules appear slightly thinner, indicative of interactions of the molecules with the substrate. The described graphene templating technique should be broadly applicable to other systems.

2.5 Figures
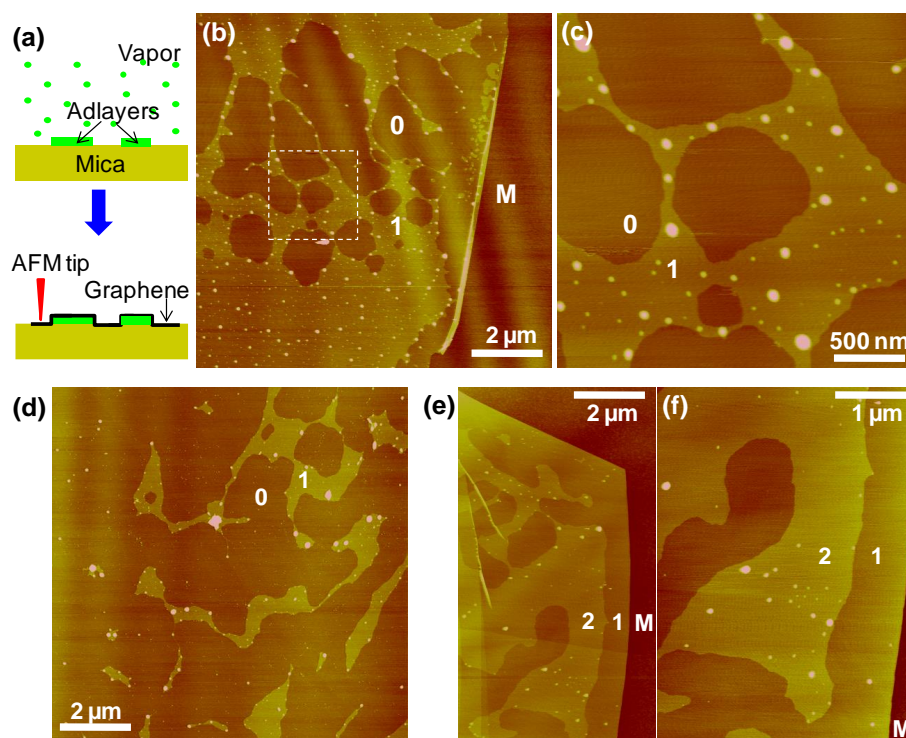
Figure 1- AFM images of graphene-templated THF adlayers, taken within a few hours after graphene sheets were deposited. **(a):** Schematic of the graphene templating technique. **(b)**: The case in which the trapped adlayer is a submonolayer. **(c):** Zoom-in of the square in (b). **(d):** Another sample with very low surface coverage of THF. **(e):** Another sample, showing the second THF adlayers on top of the first. **(f):** Zoom-in of the second adlayer in (e). M labels the mica surface, and 0, 1, and 2 label regions where monolayer graphene is on top of 0, 1, and 2 adlayers of THF, respectively.
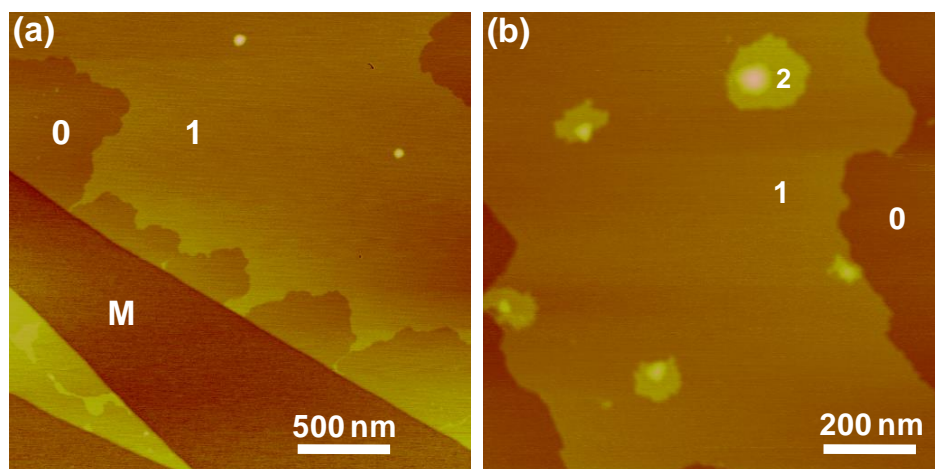
Figure 2 – AFM images of graphene-templated cyclohexane adlayers, taken within a few hours after graphene was deposited. **(a):** A typical image of graphene-templated submonolayer of cyclohexane adlayer. **(b):** Another sample showing the second cyclohexane adlayers. M labels the mica surface, and 0, 1, and 2 label regions where monolayer graphene is on top of 0, 1, and 2 adlayers of cyclohexane, respectively.
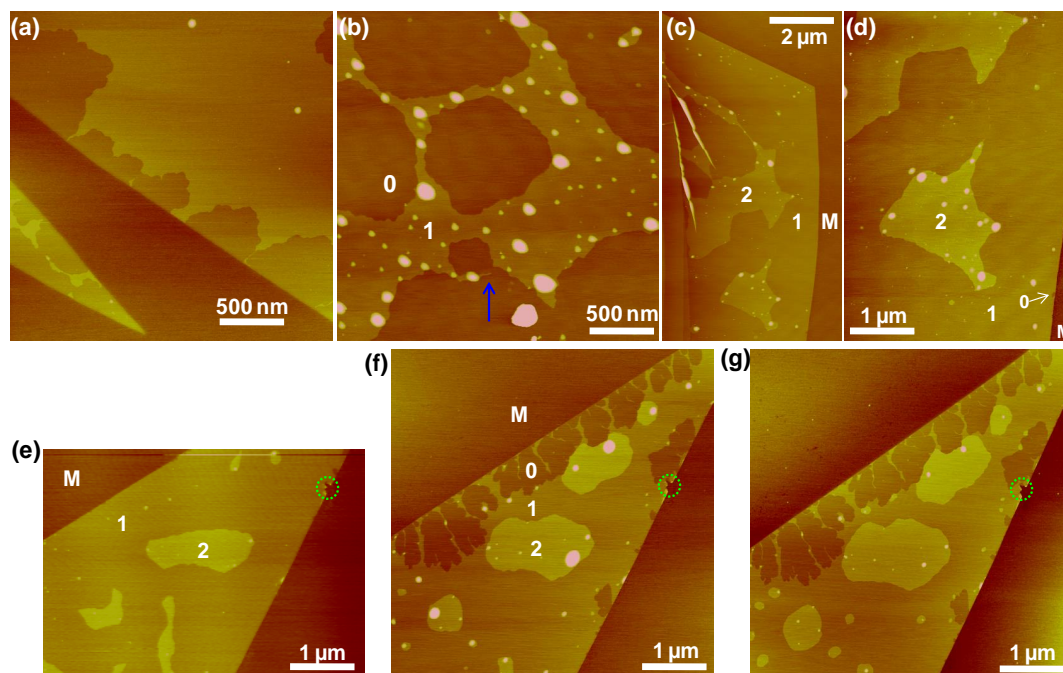
Figure 3 – Dynamics of the graphene-templated adlayers of cyclohexane and THF. **(a):** A representative cyclohexane sample (Fig. 2a) after being kept at ambient conditions for 2 months. **(b-d):** THF samples after being kept at ambient conditions for 2 months, corresponding to Fig 1c,e,f, respectively. **(e-g):** Another THF sample freshly after prepared (e), and after being kept at ambient conditions for 60 days (f) and 68 days (g). The green circle marks a defect on the graphene edge, which served as a reference point in aligning the images. M labels the mica surface, and 0, 1, and 2 label regions where monolayer graphene is on top of 0, 1, and 2 adlayers of THF, respectively.
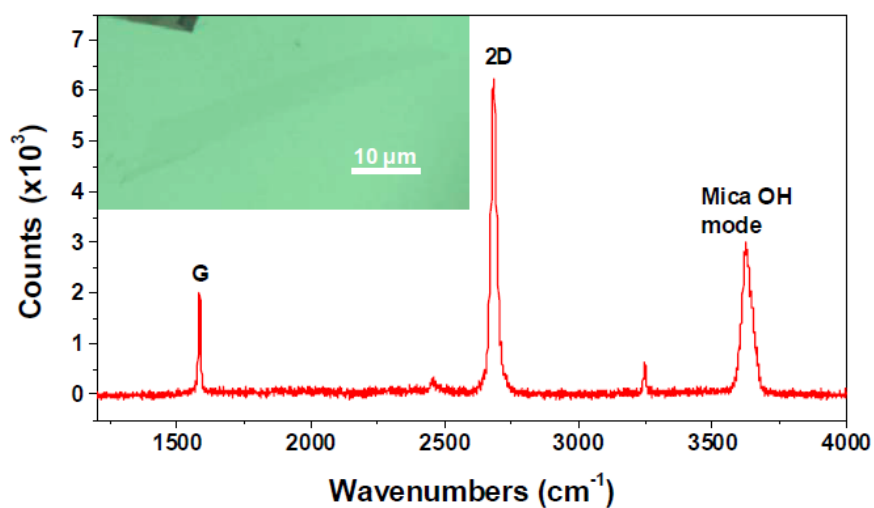
Figure 4 – Raman spectrum of a monolayer graphene sheet deposited on a mica surface that was in equilibrium with THF vapor. Inset: transmission optical image of the graphene sheet at the center. The 2D and G bands of graphene and the OH mode of mica are labeled. Similar Raman spectra were also observed for monolayer graphene sheets deposited on mica surfaces that were in equilibrium with cyclohexane vapors.

2.6 References

1. Weaver, J. F.; Carlsson, A. F.; Madix, R. J. The adsorption and reaction of low molecular weight alkanes on metallic single crystal surfaces. *Surf. Sci. Rep.* **2003**, *50*, 107.

2. Goss, K. U. The air/surface adsorption equilibrium of organic compounds under ambient conditions. *Crit. Rev. Environ. Sci. Technol.* **2004**, *34*, 339.

3. Bruch, L. W.; Diehl, R. D.; Venables, J. A. Progress in the measurement and modeling of physisorbed layers. *Rev. Mod. Phys.* **2007**, *79*, 1381.

4. Beaglehole, D.; Christenson, H. K. Vapor adsorption on mica and silicon - entropy effects, layering, and surface forces. *J. Phys. Chem.* **1992**, *96*, 3395.

5. Xu, L.; Salmeron, M.; Bardon, S. Wetting and molecular orientation of 8CB on silicon substrates. *Phys. Rev. Lett.* **2000**, *84*, 1519.

6. Xu, L.; Ogletree, D. F.; Salmeron, M.; Tang, H. A.; Gui, J.; Marchon, B. De-wetting of lubricants on hard disks. *J. Chem. Phys.* **2000**, *112*, 2952.

7. Lazar, P.; Schollmeyer, H.; Riegler, H. Spreading and two-dimensional mobility of long-chain alkanes at solid/gas interfaces. *Phys. Rev. Lett.* **2005**, *94*, 116101.

8. Riegler, H.; Kohler, R. How pre-melting on surrounding interfaces broadens solid-liquid phase transitions. *Nat. Phys.* **2007**, *3*, 890.

9. Trogisch, S.; Simpson, M. J.; Taub, H.; Volkmann, U. G.; Pino, M.; Hansen, F. Y. Atomic force microscopy measurements of topography and friction on dotriacontane films adsorbed on a SiO_2 surface. *J. Chem. Phys.* **2005**, *123*, 154703.

10. Cisternas, E. A.; Corrales, T. P.; del Campo, V.; Soza, P. A.; Volkmann, U. G.; Bai, M. J.; Taub, H.; Hansen, F. Y. Crystalline-to-plastic phase transitions in molecularly thin n-dotriacontane films adsorbed on solid surfaces. *J. Chem. Phys.* **2009**, *131*, 114705.

11. Giancarlo, L. C.; Flynn, G. W. Scanning tunneling and atomic force microscopy probes of self-assembled, physisorbed monolayers: Peeking at the peaks. *Annu. Rev. Phys. Chem.* **1998**, *49*, 297.

12. Firment, L. E.; Somorjai, G. A. Surface-structures of normal paraffins and cyclohexane monolayers and thin crystals grown on (111) crystal-face of platinum - low-energy electron-diffraction study. *J. Chem. Phys.* **1977**, *66*, 2901.

13. Firment, L. E.; Somorjai, G. A. Low-energy electron-diffraction study of surface of thin crystals and monolayers of normal paraffins and cyclohexane on Ag(111) crystal-surface. *J. Chem. Phys.* **1978**, *69*, 3940.

14. Xu, K.; Cao, P.; Heath, J. R. Graphene visualizes the first water adlayers on mica at ambient conditions. *Science* **2010**, *329*, 1188.

15. Hu, J.; Xiao, X. D.; Ogletree, D. F.; Salmeron, M. Imaging the condensation and evaporation of molecularly thin-films of water with nanometer resolution. *Science* **1995**, *268*, 267.

16. Verdaguer, A.; Sacha, G. M.; Bluhm, H.; Salmeron, M. Molecular structure of water at interfaces: Wetting at the nanometer scale. *Chem. Rev.* **2006**, *106*, 1478.

17. David, W. I. F.; Ibberson, R. M. A reinvestigation of the structure of tetrahydrofuran by high-resolution neutron powder diffraction. *Acta Crystallogr. Sect. C-Cryst. Struct. Commun.* **1992**, *48*, 301.

18.   Luger, P.; Buschmann, J. Twist conformation of tetrahydrofuran in the crystal. *Angew. Chem.-Int. Edit. Engl.* **1983**, *22*, 410.

19.   Dziubek, K. F.; Jeczminski, D.; Katrusiak, A. Pressure-generated hydrogen bonds and the role of subtle molecular features in tetrahydrofuran. *J. Phys. Chem. Lett.* **2010**, *1*, 844.

20.   Ulman, A. Formation and structure of self-assembled monolayers. *Chem. Rev.* **1996**, *96*, 1533.

21.   Kahn, R.; Fourme, R.; Andre, D.; Renaud, M. Crystal structures of cyclohexane I and II. *Acta Crystallogr. Sect. B-Struct. Commun.* **1973**, *B 29*, 131.

22.   Shigematsu, K.; Hondo, H.; Kumagai, T.; Takahashi, Y. Pressure Effect on the Solid I-Liquid and Solid III-Solid I Equilibrium Forms of Cyclohexane. *Cryst. Growth Des.* **2009**, *9*, 4674.

23.   Zinkeallmang, M.; Feldman, L. C.; Grabow, M. H. Clustering on surfaces. *Surf. Sci. Rep.* **1992**, *16*, 377.

24.   Venables, J. A.; Spiller, G. D. T.; Hanbucken, M. Nucleation and growth of thin-films. *Rep. Prog. Phys.* **1984**, *47*, 399.

25.   Evans, J. W.; Thiel, P. A.; Bartelt, M. C. Morphological evolution during epitaxial thin film growth: Formation of 2D islands and 3D mounds. *Surf. Sci. Rep.* **2006**, *61*, 1.

26.   Liu, Y. D.; Zhang, Y.; Wu, G. Z.; Hu, J. Coexistence of liquid and solid phases of Bmim-PF_6 ionic liquid on mica surfaces at room temperature. *J. Am. Chem. Soc.* **2006**, *128*, 7456.

27.   Strandburg, K. J. Two-dimensional melting. *Rev. Mod. Phys.* **1988**, *60*, 161.

28. Binder, K.; Sengupta, S.; Nielaba, P. The liquid-solid transition of hard discs: first-order transition or Kosterlitz-Thouless-Halperin-Nelson-Young scenario? *J. Phys.-Condes. Matter* **2002**, *14*, 2323.

29. Gasser, U.; Eisenmann, C.; Maret, G.; Keim, P. Melting of crystals in two dimensions. *ChemPhysChem* **2010**, *11*, 963.

C h a p t e r   3

The Microscopic Structure of Adsorbed Water on Hydrophobic Surfaces

Adapted with permission from Cao, P.*; Xu, K.*; Varghese, J.O.* and Heath, J.R. Microscopic Structure of adsorbed water on hydrophobic surfaces under ambient conditions. *Nano Letters*, **11**, 5581-5586 (2011). Copyright 2011 American Chemical Society.

3.1 Introduction

In the previous chapter, the use of graphene-templating to investigate organic molecules introduced between graphene sheets and mica substrates was described. We determined that changing the substrates being templated with graphene would be of particular interest in analyzing the applicability of graphene-templating to various surfaces of study. In particular, we wished to analyze graphene-templating of hydrophobic surfaces.

The interaction of water vapor with hydrophobic surfaces is poorly understood. In particular, a significant amount of water adsorbs onto hydrophobic surfaces under ambient conditions, contradicting expectations. We used graphene templating to investigate the microscopic structures of adsorbed water on hydrophobic surfaces. By employing graphene to preserve the adsorbed water, topographs were obtained through atomic force microscopy. Three well-defined hydrophobic surfaces [H-Si(111), graphite, and functionalized mica] were investigated, and water was found to adsorb as nanodroplets on all three surfaces under ambient conditions. The nanodroplet size (~10-100 nm) was largely surface-dependent, but their presence was closely associated with atomic-scale surface defects and step-edges. The adsorbed nanodroplets wetted all the hydrophobic substrates with contact angles <~10°, resulting in total water adsorption similar to what is found for hydrophilic surfaces. These results resolve the water-adsorption paradox of hydrophobic

surfaces, and point to the significant differences between surface processes at the atomic scale and in the macroscopic world.

Under ambient conditions, water adlayers are known to coat all hydrophilic surfaces and often dominate the surface behavior[1-4]. Studies of the microscopic structures of water adlayers on hydrophilic surfaces and under ambient conditions[2,5-8] have yielded deep insights into adsorption and wetting phenomena. In contrast, the interaction of water vapors with hydrophobic surfaces, while equally important, is not understood. The common wisdom is that due to the weak water-surface interaction, water on hydrophobic surfaces, at least to a first approximation, can be treated through macroscopic considerations, i.e., water in equilibrium with its vapor[4]. At equilibrium, an isolated, macroscopic droplet of water would completely evaporate into the ambient environment as long as the relative humidity (RH) is <100%. Since the attraction between water molecules and a hydrophobic surface is weaker than the self-interaction between water molecules, water droplets on hydrophobic surfaces would similarly completely evaporate – thus *no* adsorption should take place at equilibrium.

Recent experiments, however, have indicated that a significant amount of water is adsorbed on hydrophobic surfaces under ambient conditions[9,10]. Notably, the adsorbed amount of water on wax-coated, hydrophobic glass surfaces was actually found to be *higher* than that on hydrophilic glass surfaces[10]. One possible explanation is that water may aggregate as micro-droplets on hydrophobic surfaces; thus the water-covered area is small while the total adsorbed amount is high[9]. This hypothesis is supported by computer simulations[9,11]. Alternative explanations have included, for example, that the surfaces in question were porous, and so led to water absorption (rather than adsorption)[10]. The

existing results were obtained from macroscopic studies averaged over large areas of surfaces, and so no direct, microscopic evidence has been provided for the presence of micro (or nano)-droplets. In particular, the size and location of such microdroplets can potentially yield clues as to their origin. Such microscopic/nanoscale information would facilitate our understanding of the water/hydrophobic surface interface.

Here we report on the use of graphene templating[8,12] to investigate the microscopic structures of adsorbed water on hydrophobic surfaces. By employing graphene sheets to preserve and template the adsorbed water, we provide direct topographs of the system through atomic force microscopy (AFM), and we investigate water adsorption on three distinct hydrophobic surfaces: H-terminated Si(111), highly-oriented pyrolytic graphite (HOPG), and trimethylchlorosilane (TMCS)-functionalized mica. We find that the hypothesized "micro-droplets" on hydrophobic surfaces do exist, but in fact are actually "nanodroplets". They range between ~10-100 nm in size, with an average size that is highly surface dependent. However, on all surfaces studied, their occurrence is closely associated with atomic-scale surface defects and step-edges, thus resolving at least one major question associated with water adsorption on hydrophobic surfaces. Furthermore, we show that the nanodroplets wet hydrophobic surfaces well, thus indicating that surface processes at the atomic scale are guided by completely different physics when compared to the macroscopic world.

3.2 Experimental Methods

Preparation of the hydrophobic surfaces.

Hydrogen-terminated silicon(111) surfaces. The substrates used were Sb-doped, *n*-type Si

wafers with a low miscut angle of ±0.5° and a resistivity of 0.005-0.02 ohm·cm. Each Si

wafer was cut into samples of approximately 1 cm × 1 cm. A standard RCA cleaning

process was then carried out. Briefly, the substrates were immersed in a basic peroxide

solution composed of 1:1:4 by volume of 28% $NH_3·H_2O(aq)$/30% H_2O_2/H_2O at 80°C for

approximately 10 min, and then rinsed thoroughly in running Milli-Q water. H-terminated

Si(111) surface was then formed after immersing the cleaned samples in 40% NH_4F for

about 15 min. This procedure produces large, atomically flat terraces.

Trimethylchlorosilane (TMCS)-functionalized mica. Mica surface functionalization was

carried out through a vapor deposition process. Freshly cleaved muscovite mica (Grade V1;

round disks of diameter 10 mm, Ted Pella) surfaces were first exposed to an environment

with controlled relative humidity (RH) of 35±2% for about 5-10 min. The mica substrates

were then quickly transferred into a sealed reaction vessel containing a beaker filled with

~5 ml of purified TMCS liquid and allowed to react for about 30-60 min. After TMCS-

functionalization, the contact angle of the mica surface increased from ~0° to ~40°.

Graphite surfaces were prepared by freshly peeling off the top few layers of graphite from

a HOPG surface using Scotch tape.

Graphene templating of water adlayers on surfaces. Graphene sheets were prepared by

the standard method of mechanical exfoliation[14,42] of Kish graphite onto the

abovementioned surfaces. A few flakes of graphite are placed on a piece of Scotch-tape

which is repeatedly closed on itself and then opened. The resulting graphite-covered tape is

then pressed down onto the various substrates, leaving flakes of various thicknesses on the

surface. All experiments were performed at room temperature (22±2 °C). Humidity was monitored using a Fluke 971 temperature humidity meter. For graphene deposition at ambient conditions, the ambient RH was measured to be in a range of 36% to 42% for all experiments. The samples were allowed to equilibrate with the ambient environment for about 5 min before graphene was deposited. Low humidity (<3% RH) experiments were carried out in a glove-bag (Sigma-Aldrich AtmosBag) that was purged and protected under a continuous flow of ultra-high purity argon. The graphite surfaces were prepared inside the glove-bag and again allowed to equilibrate with the environment of controlled RH for ~5 min before graphene was deposited.

Identification of graphene layers. Graphene mono- and few-layers were identified through optical microscopy and confirmed by spatially resolved Raman spectroscopy. In the optical search process, we found it was easier to identify the thinnest graphene sheets on TMCS-functionalized mica using transmitted light. For the basal planes of HOPG, we were able to identify the edges of deposited graphene sheets through dark field scattering microscopy. In this mode, the contrast of the feature edges is enhanced. For H-terminated Si(111) surfaces, we found that the contrast of graphene sheets can be enhanced by proper filtering of the micrographs obtained from a CMOS camera. To confirm the identification of graphene layers on TMCS-functionalized mica and H-Si(111), spatially resolved Raman spectra were recorded (Figure 5). A Renishaw M1000 micro-Raman spectrometer system was used for this purpose, using a 514.5 nm laser beam and a 2400 lines per mm grating. A confocal optical microscope with a ×100 objective lens was used to record spectra with a spatial resolution of 2 μm. No noticeable D peak (~1350 cm^{-1}) was observed in the Raman

spectra of the deposited graphene, indicating high-crystalline order of our samples. The

weak peak at ~1450 cm^{-1} is attributed to the third-order optical phonon mode of the silicon

substrate[43,44].

AFM Measurements. AFM images were acquired under tapping mode on a Digital

Instrument Nanoscope IIIA at ambient conditions. A sharp TESP tip (Veeco) was used in

the experiment. Typical values for the force constant, resonance frequency and tip radius

were 42 N/m, 320 kHz, and 8 nm, respectively. Height calibrations were performed using

the step heights of freshly cleaved graphite samples.

3.3 Results and discussion

Each of the three well-defined hydrophobic surfaces investigated here has its own

characteristic pattern of atomic defects, and so a relationship between the surface

morphology and adsorbed water structures can be established. We previously reported the

use of graphene templating for studying adsorption processes of water and small organic

molecules on (hydrophilic) mica surfaces[8,12], and, more recently, graphene templating of

single DNA molecules has also been demonstrated on mica substrates[13]. However, the

generalization of this technique to hydrophobic substrates is non-trivial. Particularly, the

technique relies on the identification of graphene sheets deposited on atomically flat

surfaces that are in equilibrium with the vapors of interest[8,12]. This can be a daunting task,

considering graphene is only a single layer of carbon. For the basal planes of HOPG, we

identified the edges of deposited graphene sheets through dark field scattering microscopy.

For H-terminated Si(111) surfaces, we found the contrast of graphene sheets can be

enhanced by proper filtering of the micrographs obtained from a CMOS camera. For

surface-functionalized mica surfaces, we found the optical properties of the substrate are

not noticeably affected by surface-functionalization, so graphene sheets can be identified,

as reported previously, through optical microscopy[8,14]. The identification of deposited

graphene on all three substrates permitted the extension of the graphene templating

technique to hydrophobic surfaces.

Fig. 1a.b shows the results we obtained on HOPG surfaces under ambient

conditions (~40% RH). After graphene-templating, droplet-like structures are observed

across the samples where the HOPG surface is covered under the deposited graphene

sheets. Meanwhile, no droplets were observed on bare HOPG surfaces without graphene

coverage. RH-dependent experiments indicate that both the number density and the sizes of

the droplets are reduced for samples prepared at low RH (Fig 1c), confirming that the

observed droplets are adsorbed water. These results demonstrate that the graphene-

templating method can lock down the otherwise highly diffusive water molecules, thus

permitting a mapping of the adsorbed water on the HOPG surface.

The very large majority of the observed droplets are lined up along the step edges

of the HOPG substrate (A,B in Fig. 1b), with droplets rarely observed over the large terrace

areas (C in Fig. 1b). The droplets are typically 100-300 nm in lateral dimensions, 5-15 nm

in height (hence "nanodroplets"), and slightly elongated along the edges. Larger, highly

elongated nanodroplets spreading along the edges are also occasionally observed (A in Fig.

1b). The exact height varies, and is not a multiple of the bilayer height in ice crystals (0.37

nm)[15], implying that the adsorbed water nanodroplets are liquid-like. In contrast, we

previously found that water adsorbs as crystal-like adlayers on hydrophilic mica surfaces at

room temperature[5,6,8], forming mesa-like structures with the exact height of the ice

crystals[8]. The nanodroplets appear somewhat self-organized; an averaged nanodroplet-to-nanodroplet separation of ~450 nm was measured at ~40% RH (Fig. 1b inset). A previous study of droplets from a KOH solution deposited on HOPG surfaces also found a nearly uniform distribution of droplets along step edges[16].

Our results indicate that on the hydrophobic graphite surfaces (contact angle of water ~90°)[17-19], nanodroplets 5-15 nm in height are apparently nucleated at the 0.335 nm high step edges of graphite. This observation demonstrates that atomic scale defects, which are present even in the most ideal cases, play significant roles in determining adsorption and wetting properties. By integrating the heights of all the adsorbed water nanodroplets, we found that the total amount of surface adsorbed water at 40% RH (as in Fig. 1b) is ~73% of a monolayer. In comparison, using the same integration method, the amount of water adsorbed on a hydrophilic mica surface at 40% RH is ~45% of a monolayer. Thus, the step-induced nucleation of nanodroplets on HOPG leads to a highly hydrophobic surface that adsorbs more water than the model hydrophilic surface of clean mica.

Fig. 2 presents the results for H-terminated Si(111)[20], which is another well-characterized hydrophobic surface (contact angle of water ~90°)[21,22]. After graphene templating, nanodroplets are again revealed across the surface. Similar to the case for HOPG, the nanodroplets are observed along step edges, but considerable numbers of nanodroplets are also observed on the terraces (Fig. 2ab). By comparing with atomically-resolved scanning tunneling microscope images (Fig. 2c), we infer that the water nanodroplets on the terraces could be assigned to etch pits, a class of atomic defects that are hard to avoid during the wet-chemistry preparation of H-terminated Si(111)[23]. These etch pits, which are typically only a single atomic layer in depth and a couple of nanometers

across, are also roughly recognizable in the AFM images for areas without graphene

coverage (Fig. 2a). Like the step edges, these atomic scale defects are apparently also

capable of nucleating water nanodroplets that are much larger than the defect sizes. The

originally concave etch pits (Fig. 2ac) become convex (Fig. 2ab) in the topographs when

the adsorbed nanodroplets are preserved and visualized by graphene templating. Such

atomic defects are generally absent from freshly cleaved HOPG surfaces[24], which is

consistent with our observation that nanodroplets on HOPG are almost always at the terrace

edges. On the H-terminated Si(111) surface, the nanodroplets are ~10-20 nm in lateral

dimensions, and 0.3-0.5 nm in height. Direct height integration indicates that the amount of

adsorbed water (~15% of a monolayer coverage) is lower than that which adsorbs on

hydrophilic mica surfaces under similar conditions. Adsorbed water nanodroplets could

help explain the recent experimental finding that water vapor appears to significantly affect

the conductivity of H-terminated silicon-on-oxide(111) surfaces[25].

Organically-functionalized mica surfaces represent a third interesting hydrophobic

surface. Freshly cleaved mica surfaces are hydrophilic, but can be made hydrophobic

through silanization[26-28]. Fig. 3 presents the graphene-templating results obtained on mica

surfaces functionalized by trimethylchlorosilane (TMCS). TMCS treatment modifies the

surface hydroxyl groups into methyl groups (Fig. 3e), and the surface property changes

from highly hydrophilic (contact angle of water ~0°) to moderately hydrophobic (contact

angle of water ~40°). Nanodroplets are again observed under graphene-covered areas (Fig.

3a), which is similar to the other hydrophobic surfaces investigated in this study, but

fundamentally different from the atomically-flat islands observed for water adsorbed on the

hydrophilic mica surface[5,8]. The nanodroplets are 20-40 nm in lateral dimensions and 0.5-

1.5 nm in height, and distribute uniformly across the surface (Fig. 3b). A close-up

inspection of the TMCS-functionalized mica surface itself (Fig. 3c) indicates that the

surface is characterized by randomly distributed inhomogeneities at the atomic scale that

are not present on the freshly cleaved (non-functionalized) surface (Fig 3d). These features

are presumably defects or domain boundaries within the TMCS surface layer,[27] which

appear as features with ~10 nm lateral dimensions and 1-3 angstroms in height, and are

observed across the entire surface. A Fourier transform of the images (Fig. 3bc insets)

further shows that the distribution of water nanodroplets (as visualized by graphene

templating) and the distribution of domain-like structures in the TMCS-functionalized mica

surface both correspond to a characteristic length of ~75 nm in lateral dimensions (Fig. 3f).

This result suggests that, similar to the cases of HOPG and H-Si(111) surfaces, the

adsorbed nanodroplets are again associated with defects at the atomic scale. Again, local

height variations of a few angstroms are capable of nucleating much larger nanodroplets. In

comparison, no noticeable inhomogeneity is observed on freshly cleaved mica surfaces

(Fig. 3df), and water adsorbs as two-dimensional, faceted islands of monolayer ice crystals,

and nanodroplets are seldom observed at ambient conditions[8]. Volume integration of the

nanodroplets yields a ~40% monolayer coverage for the adsorbed water on the TMCS-mica

surface. This % coverage is comparable to that on hydrophilic mica surfaces, although the

surface structure of the water is very different.

Although nanodroplets are observed on all three hydrophobic surfaces, large size

differences are found for different surfaces. Statistically, the median sizes of water droplets

on HOPG, TMCS-mica, and H-Si(111) are ~45,000, 190, and 40 nm^3, respectively. One

possible explanation for the large size differences is that the chemical properties of surface

defects (including step edges) are different for the three surfaces. For example, the edge-plane sites of HOPG are known to be highly reactive[29], and so may more strongly bond water molecules.

To further interrogate the nanodroplet morphology, we have carefully analyzed the cross-sectional profiles of the nanodroplets (Fig. 4). Semispherical cap-shaped profiles are observed for all nanodroplets. One striking observation is that despite the significant size differences, similar droplet shapes and aspect ratios are retained for all three surfaces (Fig. 4a). A linear relationship is found between the height h and the basal diameters d for all nanodroplets on the HOPG and TMCS-mica surfaces (Fig. 4cd), and similar d/h ratios in the range of ~18-40 are obtained for those surfaces (Fig. 4 ef). A previous study on KOH solution nanodroplets deposited on HOPG surfaces also found the apparent diameters to be about one order of magnitude larger than the apparent heights[16]. These large d/h ratios indicate that the nanodroplets spread extremely flat on the substrates (Fig. 4b). The contact angles (θ) of the nanodroplets can be estimated[30] as $\theta = 2\arctan(2h/d)$, which yields 5-12° for both surfaces (Fig. 4 ef). For the H-Si(111) surface, the d/h ratios are less certain due to the very small sizes of nanodroplets and thus large uncertainties in profile measurements. However, a similarly small θ (~3-10°) was also obtained.

These surprisingly small θ values indicate that the water nanodroplets wet hydrophobic surfaces quite well. Recent studies on droplets of various liquids artificially deposited on solid surfaces have also found that when the droplet diameter is reduced to micrometer and sub-micrometer scales, drastically reduced θ is observed[30-33]. The reduced θ is often attributed to the effects of the contact line tension (τ), which is a one-dimensional

analogue of surface tension for solid-liquid-vapor contact lines[33-35]. Theory predicts[35-37]

that τ should have a characteristic length scale of around 1 nm, and to be on the order of 10^{-10}-10^{-11} J/m. This very small value means that quantitative measurements of τ are difficult.

Experimentally, τ can be obtained via the modified Young's equation[35], $\cos\theta = \cos\theta_o - \tau/r\gamma_L$, where θ_o is the contact angle for droplets in the macroscopic limit, r is the base radius

of the droplet, and γ_L is the liquid-vapor interfacial energy. By substituting the macroscopic

contact angles, the measured average sizes, and θ of the nanodroplets on the three surfaces,

we estimate τ to be $\sim$-6.1$\times10^{-9}$, -5.1$\times10^{-10}$ and -1.9$\times10^{-10}$ J/m for the HOPG, H-Si(111) and

TMCS-mica surfaces, respectively. These values are consistent with theory[35-37] and

previous experiments (typical range[35,38]: 10^{-8}-10^{-11} J/m).

It is surprising that we do not see a significant variation in θ with nanodroplet size,

although the influence of τ would be expected to be reduced for larger droplet sizes.

However, τ is usually defined within the context of micron- to submicron- (~100 nm) sized

droplets associated with a homogeneous surface, and defects are not explicitly incorporated

into such models. For our measurements, each nanodroplet is associated with a particular

defect (or step edge). This implies that the energy and structure of the defect, rather than

the CLT, likely make the dominant contributions to the nanodroplet size and morphology.

A second implication is that bulk-like contact angles are only observed for droplets that are

physically placed onto a macroscopic area of a surface. At equilibrium, those deposited

droplets would have evaporated. For the hydrophobic surfaces explored here, only the

defect-associated nanodroplets are observed at equilibrium. In other words, when the

surface is in equilibrium with water vapor, defect- (or step edge-) associated, low-contact

angle ($\theta < \sim 10^{\circ}$) nanodroplets dominate surface wetting.

3.4 Conclusions

Graphene templating provides a unique means to preserve and visualize the

adsorbed water structures on hydrophobic surfaces. Our results confirmed the presence of

previously hypothesized "micro-droplet" structures[9,11], with the caveat that the structures

are actually "nanodroplets" of 10-100 nm in size. Moreover, we found the occurrence of

nanodroplets is closely associated with defects at the atomic scale. For the HOPG surface,

where step edges are the only defects, nanodroplets predominantly reside along step edges.

For H-Si(111), defects are associated with both step edges and etch pits, and nanodroplets

reside at both sites. For TMCS-mica, domain-like inhomogeneity in the molecular surface

layer provides the defects for water nucleation; nanodroplets thus scatter across the surface

at the same characteristic frequency as those domains. This is in contrast to highly

hydrophilic surfaces, where previous studies have indicated that small surface defects,

including step edges, may assist in the nucleation of surface water (ice) layers[7,8,39], but

those defects do not appear to influence the total amount of adsorbed water, except, perhaps

at very low relative humidity levels.

Recent studies have also suggested that for hydrophilic surfaces, the first ice-like

water adlayer may render the surface hydrophobic[4,40,41] and so prevent subsequent water

adsorption. Our study indicates that, for hydrophobic surfaces, adsorbed water nanodroplets

are as ubiquituous as the atomic scale defects and step edges that characterize such

surfaces. Those defects apparently dominate the morphology of adsorbed water under

equilibrium conditions, so that the nanodroplets wet the surface with contact angles as small as a few degrees, thus leading to considerable total adsorption amounts. The result is that hydrophilic and hydrophobic surfaces can contain nearly equivalent amounts of adsorbed water, but for very different reasons. Our results exemplify how surface processes at the atomic scale can be completely different from the macroscopic world.

3.5 Figures
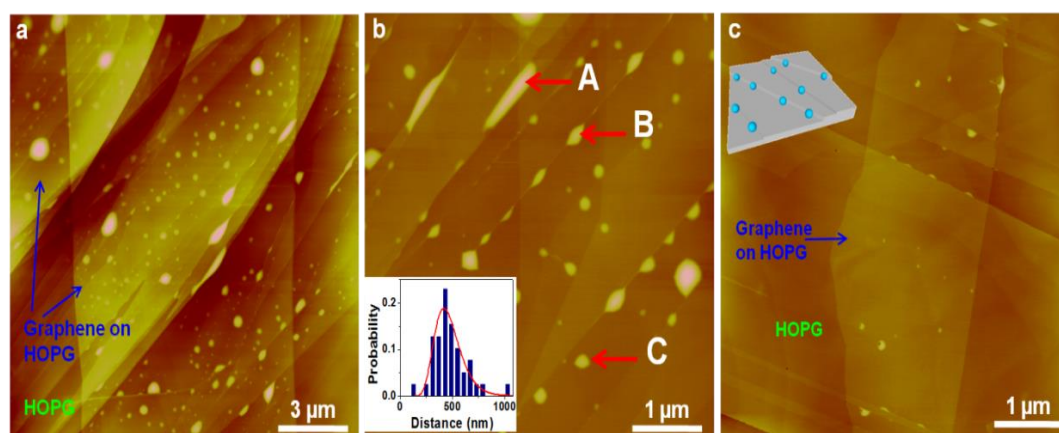
Figure 1 – Water adsorption on HOPG surfaces, visualized by graphene-templating. a and b, AFM topographic images of graphene covering HOPG surfaces under ambient conditions (~40% RH). Inset of b: distribution of separation between neighboring nanodroplets along the step edges, revealing a characteristic length scale of around 450 nm. c, Another sample prepared at <3% RH. Inset: a drawing showing that water nanodroplets (blue) mainly reside along the step edges.
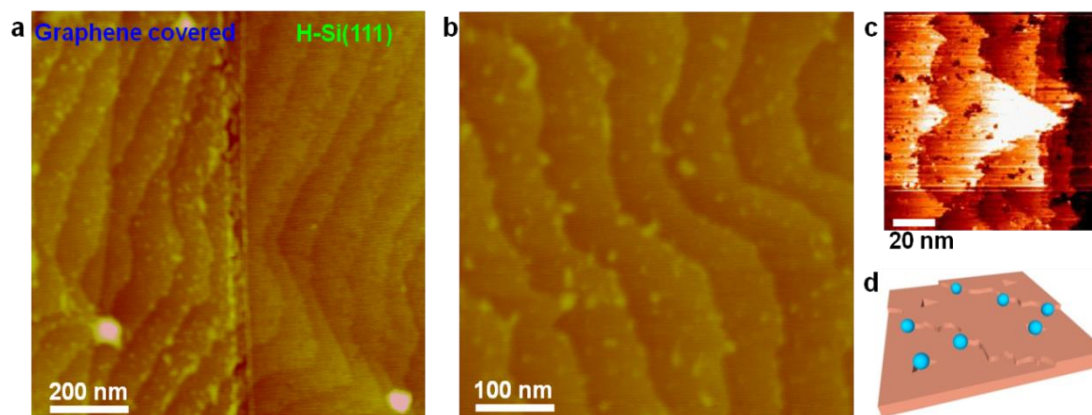
Figure 2 – Water adsorption on H-terminated Si(111) surface. a, AFM topographic image of graphene covering H-terminated Si(111) surface under ambient conditions (~40% RH). b, AFM topographic image of another graphene-templated sample. c, Low-temperature (77 K) scanning tunneling microscope topographic image of a H-terminated Si(111) surface. d, A schematic showing that water nanodroplets (blue) reside along edges and at etch pits.
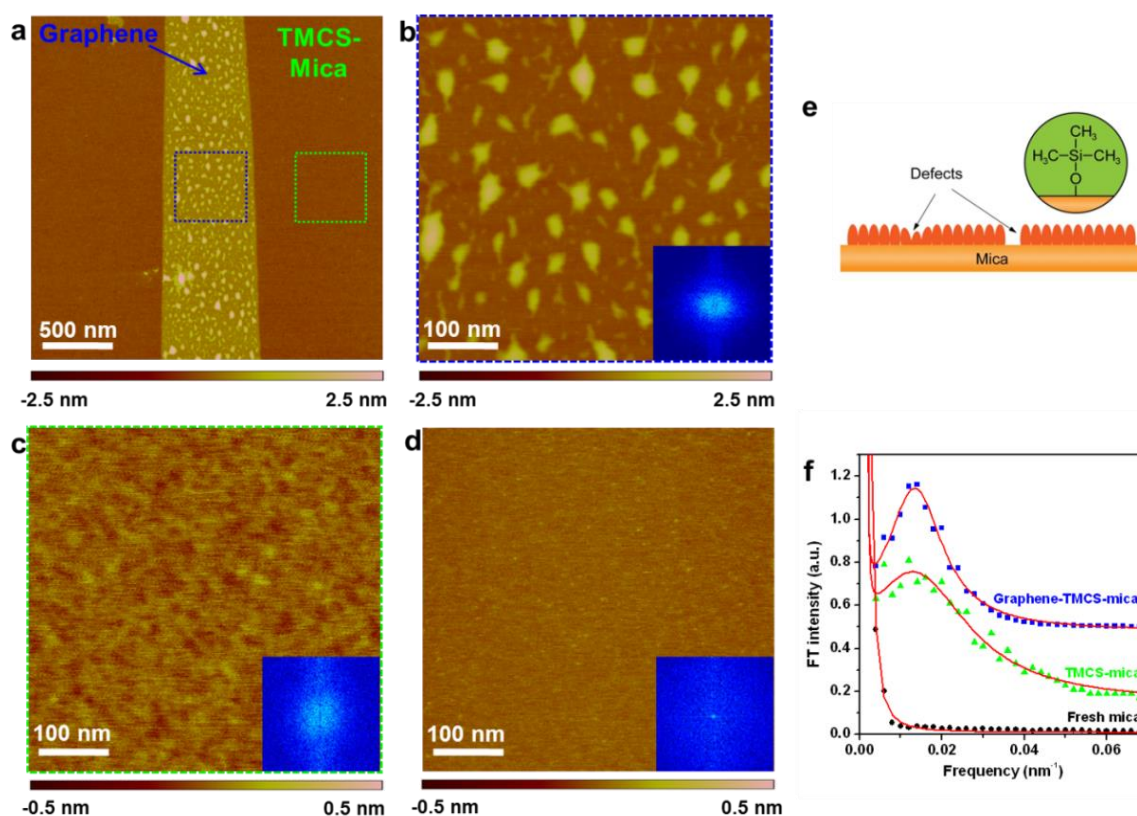
Figure 3 – Water adsorption on surface-functionalized mica. a, AFM topographic image of graphene covering TMCS-functionalized mica under ambient conditions (~40% RH). b and c, Close-up views of the areas indicated by the blue and green squares in a. d, AFM topographic image of freshly cleaved mica surface. Note the height scales for c,d are five times smaller than that for a,b. Insets in b-d: two-dimensional Fourier transform of each image. e, A drawing showing the TMCS-functionalized mica surface. f, Radial averaged intensity profiles versus frequency. Lorentzian fits are indicated by red lines. Curves are vertically displaced for clarity. Characteristic frequencies of b and c are 1.34×10^{-2} and 1.30×10^{-2} nm^{-1}, respectively, both corresponding to a characteristic length of ~75 nm.
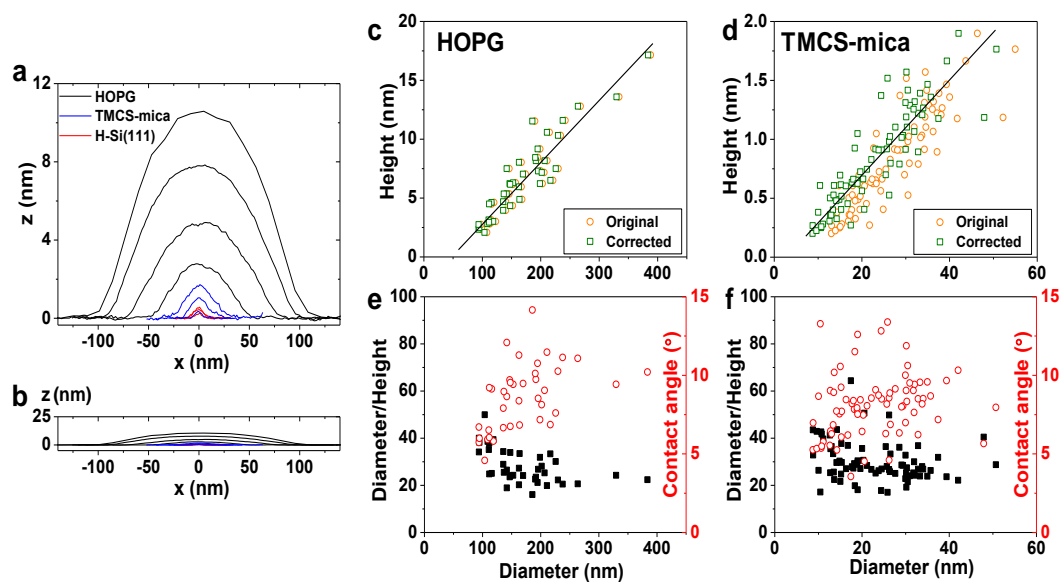
Figure 4 - Cross-sectional profiles of the nanodroplets. a, The cross-sectional profiles of typical nanodroplets observed on HOPG, TMCS-mica and H-Si(111) surfaces under ambient conditions. b, The profiles plotted on a 1:1 x-z scale. c,d, The height-diameter relationship for nanodroplets on HOPG (c) and TMCS-mica (d) surfaces. Orange circles and green squares respectively represent the original data and the data after corrected for the broadening effects due to tip radius and graphene templating[13]. e,f, The diameter/height ratios (black) and contact angles (red) for nanodroplets on the two surfaces.
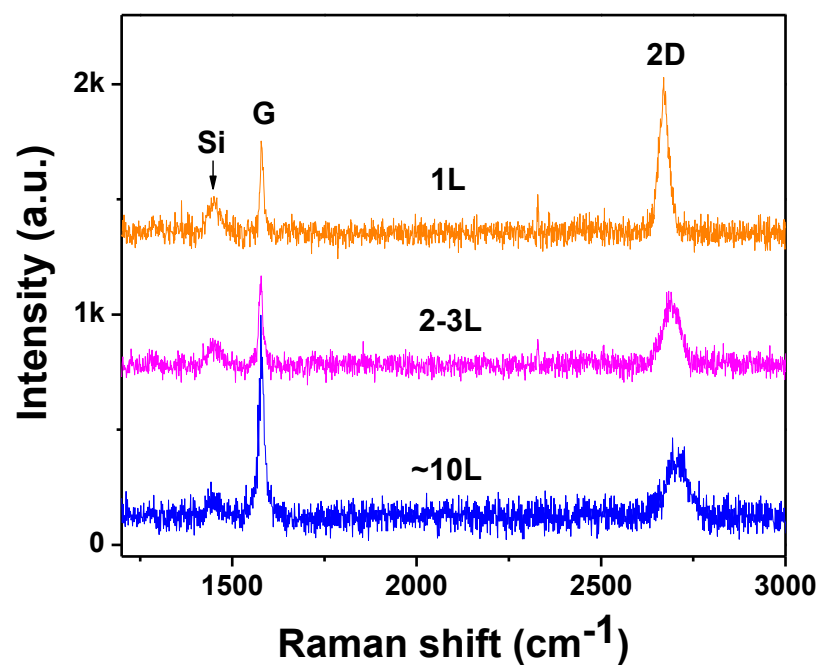
Figure 5 – Raman spectra of different layers of graphene.

3.6 References

1. Thiel, P. A. & Madey, T. E. The interaction of water with solid-surfaces: fundamental aspects. *Surf. Sci. Rep.* **7,** 211-385 (1987).

2. Verdaguer, A., Sacha, G. M., Bluhm, H. & Salmeron, M. Molecular structure of water at interfaces: Wetting at the nanometer scale. *Chem. Rev.* **106,** 1478-1510 (2006).

3. Ewing, G. E. Ambient thin film water on insulator surfaces. *Chem. Rev.* **106,** 1511-1526 (2006).

4. Feibelman, P. J. The first wetting layer on a solid. *Phys. Today* **63(2),** 34-39 (2010).

5. Hu, J., Xiao, X. D., Ogletree, D. F. & Salmeron, M. Imaging the condensation and evaporation of molecularly thin-films of water with nanometer resolution. *Science* **268,** 267-269 (1995).

6. Miranda, P. B., Xu, L., Shen, Y. R. & Salmeron, M. Icelike water monolayer adsorbed on mica at room temperature. *Phys. Rev. Lett.* **81,** 5876-5879 (1998).

7. Verdaguer, A., Cardellach, M. & Fraxedas, J. Thin water films grown at ambient conditions on $BaF_2(111)$ studied by scanning polarization force microscopy. *J. Chem. Phys.* **129,** 174705 (2008).

8. Xu, K., Cao, P. G. & Heath, J. R. Graphene visualizes the first water adlayers on mica at ambient conditions. *Science* **329,** 1188-1191 (2010).

9. Rudich, Y. *et al.* Wetting of hydrophobic organic surfaces and its implications to organic aerosols in the atmosphere. *J. Phys. Chem. A* **104,** 5238-5245 (2000).

10. Sumner, A. L. *et al.* The nature of water on surfaces of laboratory systems and implications for heterogeneous chemistry in the troposphere. *Phys. Chem. Chem. Phys.* **6,** 604-613 (2004).

11. Moussa, S. G. *et al.* Experimental and theoretical characterization of adsorbed water on self-assembled monolayers: understanding the interaction of water with atmospherically relevant surfaces. *J. Phys. Chem. A* **113,** 2060-2069 (2009).

12. Cao, P. G., Xu, K., Varghese, J. O. & Heath, J. R. Atomic force microscopy characterization of room-temperature adlayers of small organic molecules through graphene templating. *J. Am. Chem. Soc.* **133,** 2334-2337 (2011).

13. Severin, N., Dorn, M., Kalachev, A. & Rabe, J. P. Replication of single macromolecules with graphene. *Nano Lett.* **11,** 2436-2439 (2011).

14. Lui, C. H., Liu, L., Mak, K. F., Flynn, G. W. & Heinz, T. F. Ultraflat graphene. *Nature* **462,** 339-341 (2009).

15. Fletcher, N. H. *The Chemical Physics of Ice* (Cambridge Univ. Press, London, 1970).

16. Hu, J., Carpick, R. W., Salmeron, M. & Xiao, X. D. Imaging and manipulation of nanometer-size liquid droplets by scanning polarization force microscopy. *J. Vac. Sci. Technol. B* **14,** 1341-1343 (1996).

17. Werder, T., Walther, J. H., Jaffe, R. L., Halicioglu, T. & Koumoutsakos, P. On the water-carbon interaction for use in molecular dynamics simulations of graphite and carbon nanotubes. *J. Phys. Chem. B* **107,** 1345-1352 (2003).

18. Yang, D. S. & Zewail, A. H. Ordered water structure at hydrophobic graphite interfaces observed by 4D, ultrafast electron crystallography. *Proc. Natl. Acad. Sci. U. S. A.* **106,** 4122-4126 (2009).

19. Shin, Y. J. *et al.* Surface-energy engineering of graphene. *Langmuir* **26,** 3798-3802 (2010).

20. Higashi, G. S., Chabal, Y. J., Trucks, G. W. & Raghavachari, K. Ideal hydrogen termination of the Si-(111) surface. *Appl. Phys. Lett.* **56,** 656-658 (1990).

21. Silvestrelli, P. L., Toigo, F. & Ancilotto, F. Interfacial water on Cl- and H-terminated Si(111) surfaces from first-principles calculations. *J. Phys. Chem. B* **110,** 12022-12028 (2006).

22. Lange, B. *et al.* Water adsorption on hydrogenated Si(111) surfaces. *Surf. Sci.* **603,** 60-64 (2009).

23. Wade, C. P. & Chidsey, C. E. D. Etch-pit initiation by dissolved oxygen on terraces of H-Si(111). *Appl. Phys. Lett.* **71,** 1679-1681 (1997).

24. Chang, H. P. & Bard, A. J. Observation and characterization by scanning tunneling microscopy of structures generated by cleaving highly oriented pyrolytic-graphite. *Langmuir* **7,** 1143-1153 (1991).

25. Dubey, G., Lopinskia, G. P. & Rosei, F. Influence of physisorbed water on the conductivity of hydrogen terminated silicon-on-insulator surfaces. *Appl. Phys. Lett.* **91,** 232111 (2007).

26. Kessel, C. R. & Granick, S. Formation and characterization of a highly ordered and well-anchored alkylsilane monolayer on mica by self-assembly. *Langmuir* **7,** 532-538 (1991).

27.   Schwartz, D. K., Steinberg, S., Israelachvili, J. & Zasadzinski, J. A. N. Growth of a self-assembled monolayer by fractal aggregation. *Phys. Rev. Lett.* **69,** 3354-3357 (1992).

28.   Xiao, X. D., Liu, G. Y., Charych, D. H. & Salmeron, M. Preparation, structure, and mechanical stability of alkylsilane monolayers on mica. *Langmuir* **11,** 1600-1604 (1995).

29.   Banks, C. E., Davies, T. J., Wildgoose, G. G. & Compton, R. G. Electrocatalysis at graphite and carbon nanotube modified electrodes: edge-plane sites and tube ends are the reactive sites. *Chem. Commun.*, 829-841 (2005).

30.   Wang, R. G., Cong, L. & Kido, M. Evaluation of the wettability of metal surfaces by micro-pure water by means of atomic force microscopy. *Appl. Surf. Sci.* **191,** 74-84 (2002).

31.   Rieutord, F. & Salmeron, M. Wetting properties at the submicrometer scale: A scanning polarization force microscopy study. *J. Phys. Chem. B* **102,** 3941-3944 (1998).

32.   Checco, A., Guenoun, P. & Daillant, J. Nonlinear dependence of the contact angle of nanodroplets on contact line curvature. *Phys. Rev. Lett.* **91,** 186101 (2003).

33.   Mendez-Vilas, A., Jodar-Reyes, A. B. & Gonzalez-Martin, M. L. Ultrasmall liquid droplets on solid surfaces: production, imaging, and relevance for current wetting research. *Small* **5,** 1366-1390 (2009).

34.   de Gennes, P. G. Wetting: statics and dynamics. *Rev. Mod. Phys.* **57,** 827-863 (1985).

35.   Drelich, J. The significance and magnitude of the line tension in three-phase (solid-liquid-fluid) systems. *Colloid Surf. A-Physicochem. Eng. Asp.* **116,** 43-54 (1996).

36.   Getta, T. & Dietrich, S. Line tension between fluid phases and a substrate. *Phys. Rev. E* **57,** 655-671 (1998).

37.   Amirfazli, A. & Neumann, A. W. Status of the three-phase line tension. *Adv. Colloid Interface Sci.* **110,** 121-141 (2004).

38.   Pompe, T. & Herminghaus, S. Three-phase contact line energetics from nanoscale liquid surface topographies. *Phys. Rev. Lett.* **85,** 1930-1933 (2000).

39.   Cardellach, M., Verdaguer, A., Santiso, J. & Fraxedas, J. Two-dimensional wetting: The role of atomic steps on the nucleation of thin water films on $BaF_2(111)$ at ambient conditions. *J. Chem. Phys.* **132,** 234708 (2010).

40.   Kimmel, G. A., Petrik, N. G., Dohnalek, Z. & Kay, B. D. Crystalline ice growth on Pt(111): Observation of a hydrophobic water monolayer. *Phys. Rev. Lett.* **95,** 166102 (2005).

41.   Hu, X. L. & Michaelides, A. Water on the hydroxylated (001) surface of kaolinite: From monomer adsorption to a flat 2D wetting layer. *Surf. Sci.* **602,** 960-974 (2008).

42.   Novoselov, K. S. *et al.* Two-dimensional atomic crystals. *Proc. Natl. Acad. Sci. U. S. A.* **102,** 10451-10453 (2005).

43.   Temple, P. A. & Hathaway, C. E. Multiphonon raman-spectrum of silicon. *Phys. Rev. B* **7,** 3685-3697 (1973).

44.   Spizzirri, P. G., in *Microscopy: Science, Technology, Applications and Education*, edited by A. Méndez-Vilas & J. Díaz (FORMATEX, Badajoz, Spain, 2010), Vol. 2, pp. 1389-1396.

C h a p t e r   4

Graphene-templating of Biomolecules

In collaboration with Peigen Cao, Ann Cheung, Steve Millward, and James R. Heath

4.1 Introduction

In the two previous chapters, the technique of graphene-templating was seen to be applicable in templating various substances, as well as different substrates. Its conformation to single adlayers of materials demonstrates its unique capability to reveal surface structure at the nanoscale.[1–3] One of the best examples that we have found of this ability is its use in templating biomolecules.

Biological molecules such as DNA are among the most important molecules studied in science – they provide a wealth of information about the processes that sustain life. It is often difficult to obtain structural characteristics about such molecules. Proteins, DNA, bacteriophages, and other biomolecules are particularly susceptible to degradation by environmental factors. These include pH, temperature, concentrations of salts in the carrier solvents, and others.[4,5] Techniques such as x-ray crystallography can yield much information about these molecules, but can be quite difficult to perform. In x-ray crystallography, for example, suitable crystals of the molecules must first be made – a task that can be challenging depending on the nature of the species to be crystallized.[6–8] Scanning probe microscopy can yield high-quality images of biomolecules, but their relatively soft character can result in their being damaged by the probe tip during imaging. Here we use graphene as a template to protect the biological molecules from the scanning

probe tip, while allowing high-resolution imaging due to its conformity to the molecules. It also allows one to image the carrier solvent and its interaction with the molecules, since the graphene can effectively template the solvent as well.

4.2 Experimental Methods

A graphene-covered piece of scotch-tape was first prepared using Kish graphite flakes, and set aside for later exfoliation onto mica substrates. Solutions of two types of biomolecules, plasmid DNA and M13 bacteriophage, were prepared in water and desalted. The concentrations of both solutions were diluted to approximately 1 μG/mL, after which they were pipetted onto mica substrates. The substrates were then blown dry with nitrogen. The previously prepared graphene-covered tape was then used to exfoliate graphene onto the mica disks, and an optical microscope was used to find suitable few-layer samples of graphene. AFM measurements were performed using a Digital Instruments Nanoscope IIIa operated in Tapping Mode. Bruker TESP tips were used with a tip radius of 8 nm, force constant of 40 N/m, and resonant frequency of 320 kHz.

4.3 Results and Discussion

We found that graphene displays remarkable fidelity in conforming to both M13 bacteriophage and plasmid DNA. Figure 1 displays an AFM image of M13 bacteriophages covered by graphene, and without graphene. The structures are clearly resolved in both graphene-covered and non-graphene-covered regions of the sample. Moreover, additional features are seen in the graphene-covered portions. Droplets of water seem to be ubiquitously present underneath the graphene surface, with larger

droplets appearing only where bacteriophages are present. Figure 2 displays plasmid DNA covered by graphene. The DNA strands are clearly resolved, and seem to display an affinity for water. Once again, large droplets are found only where the biomolecules appear, indicating that water tends to collect near the plasmids.

The ultimate goal of this work was to use scanning tunneling microscopy to obtain ultra-high-resolution images of biological molecules. STM, which can yield angstrom resolution in all spatial dimensions, could potentially provide some of the most detailed images of biomolecules that have been achieved. In AFM, angstrom resolution is achieved in the height dimension, but the resolution in the lateral dimensions is limited to a few nanometers at best. In particular, if the technique was extended to template biomolecules whose structures have not been well characterized by other methods such as x-ray crystallography, much new information would be obtained. For example, membrane proteins which are particularly difficult to crystallize could be studied by this method.[9,10] As of the date of this writing, this goal has not yet been realized.

4.4 Conclusions

We have demonstrated that graphene effectively templates biological molecules. Its conformation to their structure preserves topographic information that can be extracted via scanning probe techniques. An exciting prospect is the use of STM to image the graphene-covered biomolecules and perhaps even investigate their perturbative effects on the electronic structure of graphene.

4.5 Figures
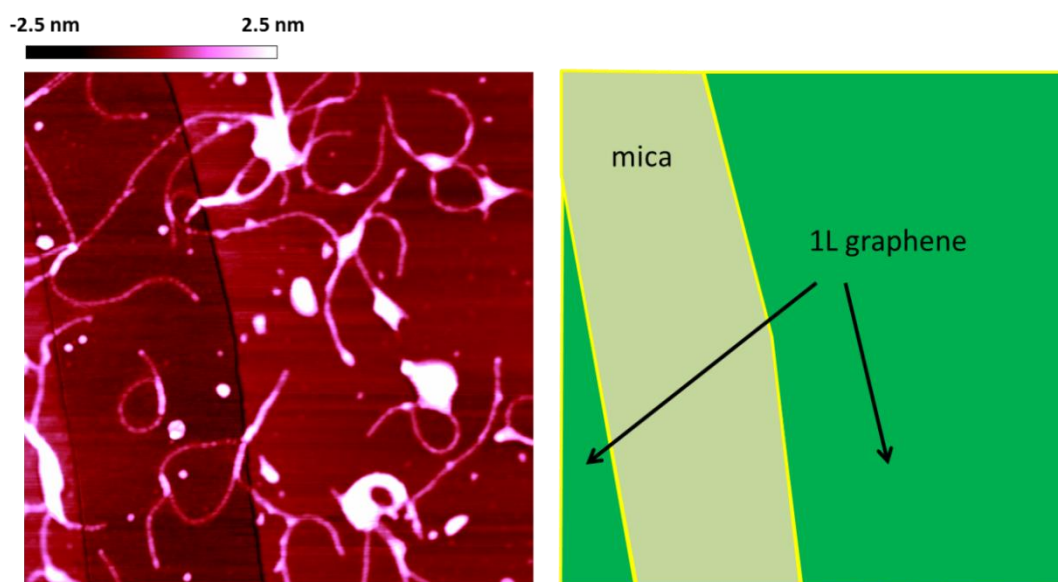
Figure 1 – Graphene-covered M13 Bacteriophage. A 2.5 μm x 2.5 μm image of M13 bacteriophage on mica – regions with graphene and without are depicted.
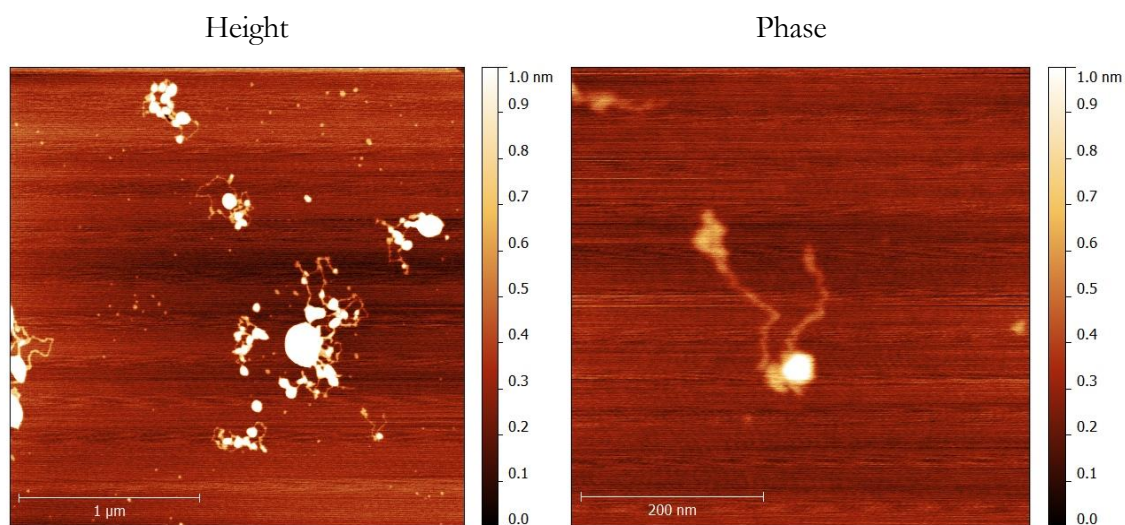
Height   Phase

Figure 2 – Graphene-covered Plasmid DNA. Topographs are taken over fully graphene-covered regions of the samples. Both height and phase images are displayed.

4.6 References

(1)   Xu, K.; Cao, P.; Heath, J. R. *Science* **2010**, *329*, 1188–1191.

(2)   Cao, P.; Xu, K.; Varghese, J. O.; Heath, J. R. *J. Am. Chem. Soc.* **2011**, *133*, 2334–2337.

(3)   Cao, P.; Xu, K.; Varghese, J. O.; Heath, J. R. *Nano Lett.* **2011**, *11*, 5581–5586.

(4)   Anderson, D. E.; Becktel, W. J.; Dahlquist, F. W. *Biochemistry (Mosc.)* **1990**, *29*, 2403–2408.

(5)   Dill, K. A.; Shortle, D. *Annu. Rev. Biochem.* **1991**, *60*, 795–825.

(6)   D'Arcy, A. *Acta Crystallogr. D Biol. Crystallogr.* **1994**, *50*, 469–471.

(7)   George, A.; Wilson, W. W. *Acta Crystallogr. D Biol. Crystallogr.* **1994**, *50*, 361–365.

(8)   Jancarik, J.; Kim, S. H. *J. Appl. Crystallogr.* **1991**, *24*, 409–411.

(9)   Levy, D.; Chami, M.; Rigaud, J.-L. *FEBS Lett.* **2001**, *504*, 187–193.

(10)   Rigaud, J.-L.; Chami, M.; Lambert, O.; Levy, D.; Ranck, J.-L. *Biochim. Biophys. Acta BBA - Biomembr.* **2000**, *1508*, 112–128.

C h a p t e r   5

Scanning-Tunneling Studies of Graphene-templated Water

5.1 Introduction

Recent studies indicate the local carrier density of graphene varies significantly at the nanometer scale due to interaction with impurities in the substrate. However, it has been difficult to correlate such spatial variations with individual impurity sites due to substrate inhomogeneity. By trapping (under graphene) nanometer-sized water clusters on the atomically well-defined Au(111) substrate, we utilize scanning tunneling microscopy (STM) and spectroscopy (STS) to characterize the local doping effects of individual water clusters on graphene. We found that water clusters, predominantly nucleated at the atomic steps of Au(111), induce strong electron doping in graphene. The doping is highly localized, and a positive correlation is observed between the water cluster size and the local doping level, in support of the recently proposed electrostatic-field-mediated doping mechanism. Our findings quantitatively demonstrate the importance of substrate-adsorbed water on the electronic properties of graphene.

As a single layer of carbon atoms, graphene[1,2] is fully comprised of surfaces. As a result, the electronic properties of graphene are significantly affected by interactions with local environments, e.g., substrates[3-8] and adsorbates.[9-13] Meanwhile, achieving control over the type and concentration of charge carriers in graphene is of both fundamental and technological importance. Previous studies have shown that the doping level of graphene

can be strongly influenced through either chemically altering the carbon lattice structure,

e.g., substitution of or bonding with carbon atoms,[14,15] or indirect electrostatic effects, e.g.,

interaction with substrates[3-8] or adsorbates.[9-13] Various techniques have been used to

characterize doping in graphene, among which STM and STS are capable of revealing

doping and electronic structure variations at the atomic and nanometer scales. For graphene

doped via substitution, STM and STS indicate that substituted nitrogen atoms locally alter

the density of states (DOS), but induce delocalized n-doping on a global scale.[15] In terms of

the indirect electrostatic effects of adsorbates and substrates, STM/STS and other studies

have observed that for graphene on SiO_2, substrate interactions lead to large variations in

local carrier density at the nanometer scale.[3-5] However, due to the large substrate

roughness and thus randomly trapped impurities and charges, it has been difficult to

correlate such spatial variations with individual impurity/inhomogeneity sites in the

substrate. At the opposite end of the spectrum, a uniform, spatially featureless local doping

level has been observed for graphene deposited on the atomically flat boron nitride

substrates.[7,8]

     In this work we use STM/STS, in combination with the graphene templating

technique,[16] to characterize the local doping effects of individual, nanometer-sized water

clusters trapped between bilayer graphene and an atomically well-defined Au(111)

substrate. We found water clusters, predominantly nucleated at the atomic steps of

Au(111), induce strong electron doping in graphene. The doping effect is highly localized,

and a strong correlation is observed between the water cluster size and the local doping

level. Previous transport studies indicated that water leads to noticeable doping for

graphene on SiO_2 substrates.[1,9] Density functional theory calculations, on the other hand,

showed no doping effects for single water molecules on freestanding graphene.[11,17] To

resolve this disagreement, an electrostatic-field-mediated doping mechanism has been

proposed based on the enhanced dipole moments of water clusters.[11,18] Our study

experimentally addresses this issue by investigating the local doping effects of individual

water clusters at the atomic and nanometer levels.

5.2 Experimental Methods

Our samples were prepared by mechanically exfoliating Kish graphite onto a

Au(111) substrate, the latter of which was pre-exposed to a controlled environment with a

~40% relative humidity for 5 minutes (Supporting Information). Graphene flakes were first

optically identified and imaged with atomic force microscopy (AFM) under ambient

conditions. For STM studies, the sample was transferred to an Omicron UHV STM system

with a base pressure of $<10^{-10}$ Torr. A mechanically cut platinum-iridium tip was used, and

the bias voltage was applied to the sample with respect to the tip.

5.3 Results and Discussion

Figure 1a shows a topographic STM image of an Au(111) substrate. Note the

increased image detail in the right hand side region; here graphene covers the Au surface.

The graphene template reveals the presence of water adsorbed along the edges of the gold

terraces, forming either isolated, droplet-like clusters or clusters connected to one another.

These water clusters ranged in size 3-5 Å in height and 10-40 nm in width. The water

clusters were likely initially adsorbed to the step edges of the gold islands under ambient

conditions,[19] while the application of graphene trapped and fixed the clusters. This is

similar to our previous AFM studies in which we utilized graphene templating to investigate the structure of water and other weakly adsorbed molecules on various surfaces.[16,19,20] Such clusters were not observed on the gold surface without graphene coverage, due to either tip-sample interactions or the possibility that the adsorbed water has evaporated in vacuum. The inset is a zoom-in of three roughly parallel steps decorated with water clusters.

The graphene atomic structure can be resolved both when the graphene is on top of an individual water cluster and when it is in direct contact with gold (Fig. 1b and c, respectively). For both areas, a triangular lattice pattern was observed and the average distance between the adjacent bright spots was ~0.25 nm, consistent with bilayer graphene possessing a Bernal stacking structure.[21] A height variation of 1-2 Angstroms over a lateral scale of 5 nm was found for both regions, indicating minimal lattice distortion for both areas. It has been recently reported that exfoliated graphene conforms to substrates with high-fidelity.[22,23] The flatness of the graphene is attributable to the atomically flat Au(111) substrate. In comparison, corrugations with amplitude of ~1 nm are typically observed when graphene is deposited on the atomically rough SiO_2 substrates.[21,24-26] The atomically flat graphene observed on top of water clusters further suggests that, at ~77 K, the water molecules under graphene cluster in an ordered, crystalline structure, rather than being amorphous.

We interrogated the influence of the trapped water clusters on the local electronic structure of graphene using STS at ~77 K to measure the local tunneling differential conductance, dI/dV. This measurement reflects the low-energy local density of states (LDOS) of the surface at the position of the STM tip. Representative spectra are shown in

Figure 1d for Au(111), graphene/Au(111), and graphene/water cluster/Au(111). The

spectrum for graphene/Au(111) was taken >20 nm away from the edges of all surrounding

water droplets. STS on the uncovered Au(111) surface shows a featureless spectrum (black

dashed line), and this spectrum is used to calibrate the LDOS of the tip. For

graphene/Au(111) and graphene/water cluster/Au(111), "U"-shaped STS spectra are

observed, with depression features (indicated by arrows) at $V_D \sim$ -75 mV and -210 mV,

respectively. Similar depression features in dI/dV have been observed in previous studies

for monolayer and bilayer graphene on both insulating and conducting substrates.[4,5,7,8,15,25]

This feature is associated with the Dirac point, where the density of states of graphene

reaches a minimum. Variations in the position of the depression feature thus reflect changes

in local doping levels. The single-position STS data in Figure 1d thus indicate that the

water cluster induced local n-doping in the graphene.

To further characterize how the water clusters affect local doping, we mapped the

spatially resolved STS spectra over a small region of the graphene-covered Au(111)

surface at 77 K (Fig. 2). The dI/dV map obtained at fixed sample-tip voltages revealed a

significant contrast within the highly localized regions where the graphene is atop the water

clusters (Fig. 2ab). As has been demonstrated for the case of graphene on SiO_2, such

contrast in the dI/dV map is directly related to variations in the local doping level.[4]

To map out the local doping level, we investigated the local energy positions of the

Dirac point ($E_D = eV_D$) by examining the positions of the depression features (V_D) in the

dI/dV curves obtained at each location. No appreciable variation in Dirac point was

observed across a graphene-covered Au(111) step where no water cluster was present (Fig.

2d,g), indicating that the step edge itself does not shift the local doping level in graphene.

The height difference between the starting point and end point is ~2.7 Å, roughly

corresponding to a single Au(111) step (2.4 Å). By contrast, a noticeable shift in the Dirac

point towards more negative sample bias is observed when the STM tip moves across

graphene-covered water clusters (Fig. 2e-g). This shift increases sharply at the cluster edge,

and flattens on the top of the cluster. Larger shifts in the Dirac point were observed for

larger water clusters. These results indicate that the shift in Dirac point is induced by the

trapped water clusters, and that this shift is dependent upon the size of the water cluster.

The local doping level can be estimated through the relationship between the Dirac

energy and the carrier concentration: $n = 4\pi E_D^2/(hv_F)^2$, where h is the Planck constant and

v_F (~10^6 m/s) is the Fermi velocity.[27] By substituting Dirac energies relative to the Fermi

level, we estimate a charge carrier density of ~4.7×10^{11} electrons per cm^2 for areas where

graphene is in direct contact with Au(111). This background doping level is on the same

order of magnitude as previously observed for graphene on copper.[15] In comparison, a

significantly enhanced doping of ~2.0×10^{12} and ~3.2×10^{12} electrons per cm^2 is estimated

for the regions atop the smaller and larger water clusters, respectively (right axis of Fig. 2g,

bottom panel).

Figure 2c presents the extracted 2D map of charge carrier density. The

homogeneous blue background, which correlates with graphene/Au(111), reflects a

spatially uniform carrier density that is in line with previous results on graphene deposited

on the atomically flat substrates of boron nitride,[7,8] but contrasts with that observed for

graphene deposited on rougher SiO$_2$ surfaces, in which large variations in local carrier

density have been ascribed to randomly trapped impurities and charges.[3-5] The additional

electron doping induced by the water clusters (red) is highly localized at the water cluster

sites with a rather small transition region (white) into the background. From these

measurements, we estimate the decay length of the local doping effect to be $< \sim 6$ nm.

The size-dependent doping effect of water clusters, as exemplified in Figure 2g,

provides additional insights into the doping mechanism. Figure 3a summarizes the

extracted average local charge carrier density as a function of the water cluster size. The

observed strong positive correlation suggests that the increasing dipole moments[28] of larger

water clusters lead to stronger local doping. Water molecules have closed-shell structures

and the HOMO and LUMO levels are more than 2 eV away from the Dirac point of

graphene. Consequently, single water molecules cannot dope freestanding graphene.[11,17]

On the other hand, clusters of water molecules possess significantly enhanced dipole

moments.[28,29] According to the recently proposed electrostatic-field-mediated doping

mechanism,[11,18] such enhanced dipole moments can induce local electrostatic fields and

lead to doping of graphene in the presence of a substrate in which the substrate-induced

impurity levels are close to the Fermi level.[11,18] The larger dipole moment enhancement of

larger clusters leads to increased local fields, thus causing stronger band shifts across the

Fermi level, hence higher local doping levels (Fig. 3b). While our data clearly demonstrate

a water cluster size effect on the doped level, the specific bands shifted by the local dipole

fields are unclear. Gold substrate-induced impurity levels in graphene and gold surface

states[30] may both contribute to this effect. Additional theoretical investigations are

necessary to clarify this point.

5.4 Conclusions

In summary, we have demonstrated that individual nanometer-sized water clusters, trapped between graphene and an Au(111) substrate, induce strong electron doping in graphene. The doping effect is highly localized at the sites of water clusters, and a strong correlation is observed between the cluster size and amount of doping. Our results support the recently proposed electrostatic-field-mediated doping mechanism, and point to the importance of substrate-adsorbed water on the electronic properties of graphene.

5.5 Figures
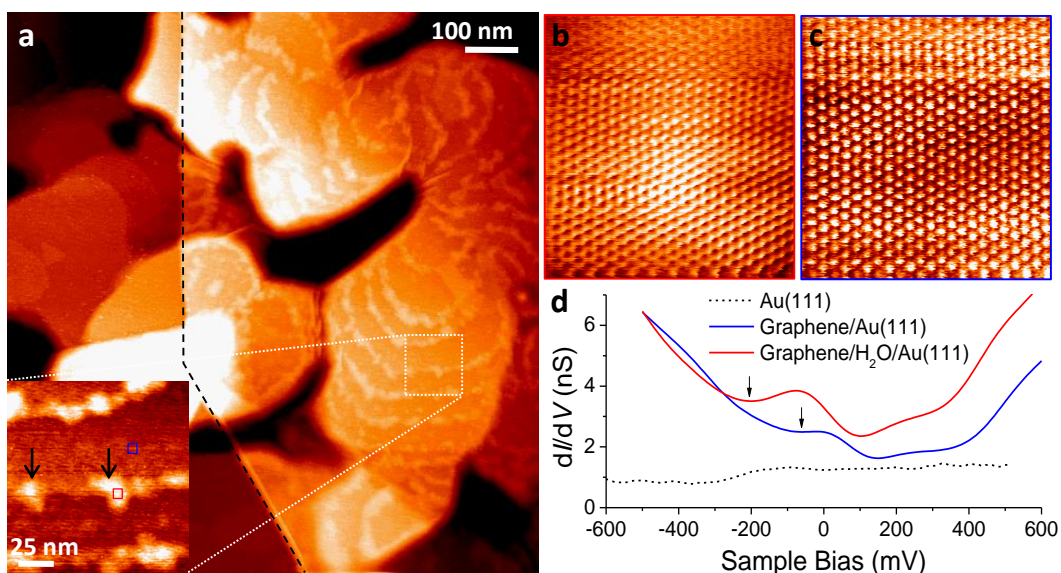
Figure 1 – STM topography and STS spectra of graphene-covered Au(111) surface. (a) A large field-of-view STM image of graphene partially covering the Au(111) substrate, taken at room temperature. Bilayer graphene [apparent height on Au(111): 0.66 nm] covers the region to the right of the dotted black line. Inset: zoom-in of the white box in the main figure. Water clusters nucleated at the gold steps appear as isolated or connected bright dots across the graphene-covered region, while such clusters are not observed on the bare Au(111) substrate. Two of these clusters are pointed to by black arrows. (b)(c) Close-up STM images (taken at ~77 K) of the red (b) and blue (c) boxes in (a), corresponding to graphene covering a water cluster on Au(111) and graphene in direct contact with Au(111), respectively. Scan size: 5×5 nm^2. The same height scale (2 Å) is used for b and c. (d) STS spectra (taken at ~77 K) of Au(111), graphene/Au(111) and graphene/H_2O/Au(111). Black arrows point to the positions of the depression features (V_D) that correspond to the Dirac point. Sample-tip bias $V_b = 0.5$ V, $I = 0.4$ nA for Au(111); $V_b = 0.13$ V, $I = 0.2$ nA for the latter two regions.
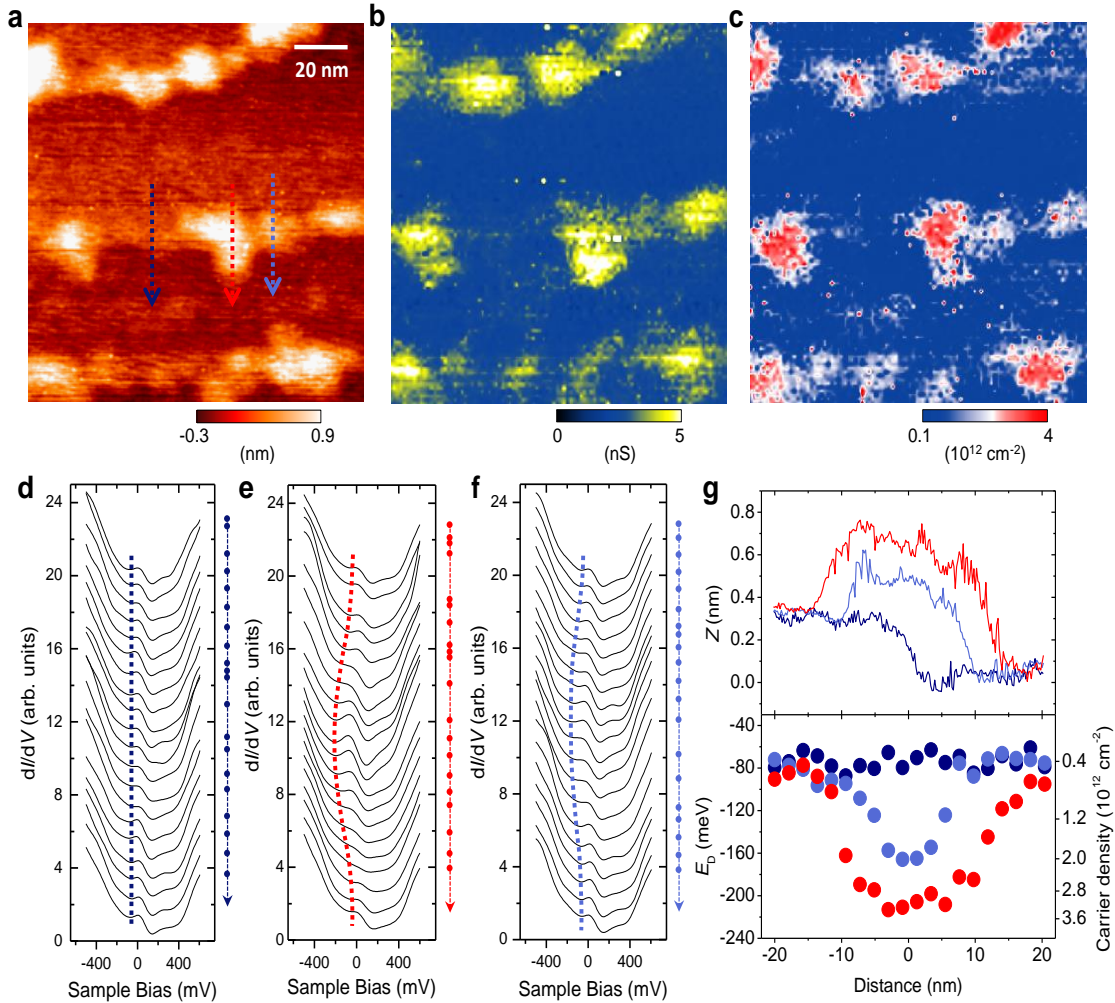
Figure 2 – Water clusters lead to highly localized doping in graphene. (a) A STM topograph of graphene-covered Au(111) surface, (white box in Fig. 1a). (b) dI/dV map of the same area at bias voltage of $V_b = 0.36$ V and 77 K. (c) Local charge carrier density map of the same area. (d) STS spectra along dark blue arrow in (a), across a graphene-covered Au step with no water. (e) STS spectra along red arrow in (a), across water cluster covered by graphene. Shift in Dirac point is tracked by the red dot line. (f) STS spectra along the light blue arrow in (a), across water cluster covered by graphene. Shift in Dirac point is tracked by the light blue dot line. (g) Upper panel: Height profiles along arrows in (a). Bottom panel: The local energy position of the Dirac point, $E_D = eV_D$, along the three arrows in (a).

a

b
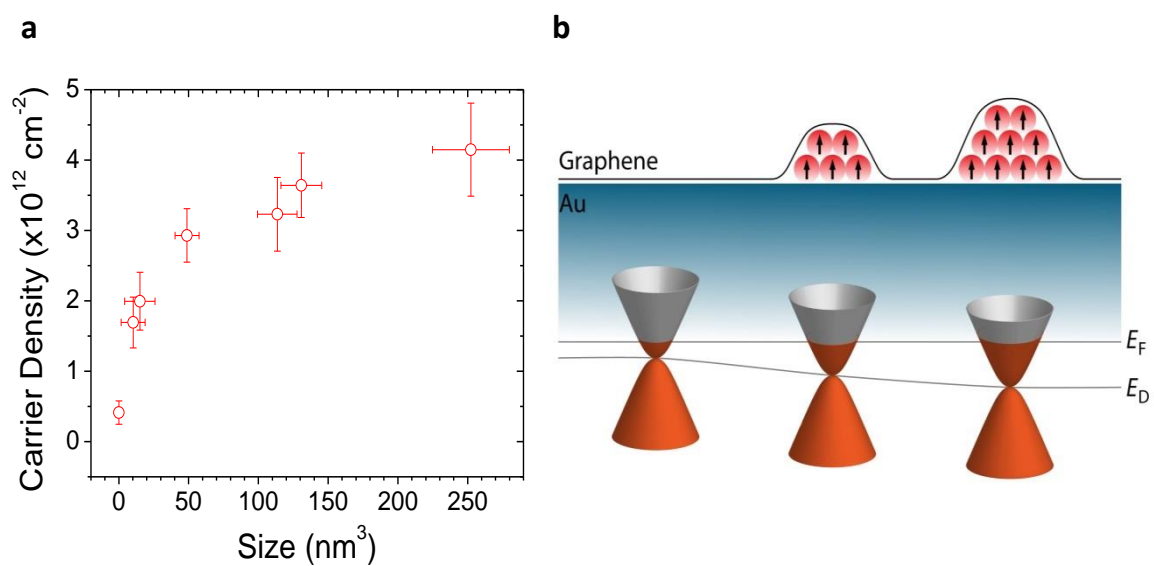
Figure 3 – Size-dependent doping effect of water clusters on graphene. (a) The measured charge carrier density as a function of water cluster size. The carrier density was averaged for graphene over the top of each water cluster. The water cluster size was obtained via numerical integration from the topographic images. (b) Schematic showing the effect of enhanced dipole moments on the shift of the Dirac point of graphene. The size of the trapped water clusters is depicted by the number of red disks. Arrows show the possible directions of the dipole moments. The structure of the actual water adlayer is not resolved here, and the dipole moments of individual water molecules depend on both the structure of ice and interactions with Au(111) and graphene. Nevertheless, the total dipole moment increases with cluster size and leads to higher doping levels.

5.6 References

1.   Novoselov, K. S.; Geim, A. K.; Morozov, S. V.; Jiang, D.; Zhang, Y.; Dubonos, S. V.; Grigorieva, I. V.; Firsov, A. A. *Science* **2004**, *306*, 666.

2.   Geim, A. K.; Novoselov, K. S. *Nat. Mater.* **2007**, *6*, 183.

3.   Martin, J.; Akerman, N.; Ulbricht, G.; Lohmann, T.; Smet, J. H.; Von Klitzing, K.; Yacoby, A. *Nat. Phys.* **2008**, *4*, 144.

4.   Zhang, Y. B.; Brar, V. W.; Girit, C.; Zettl, A.; Crommie, M. F. *Nat. Phys.* **2009**, *5*, 722.

5.   Deshpande, A.; Bao, W.; Zhao, Z.; Lau, C. N.; LeRoy, B. J. *Appl. Phys. Lett.* **2009**, *95*, 243502.

6.   Lafkioti, M.; Krauss, B.; Lohmann, T.; Zschieschang, U.; Klauk, H.; von Klitzing, K.; Smet, J. H. *Nano Lett.* **2010**, *10*, 1149.

7.   Xue, J. M.; Sanchez-Yamagishi, J.; Bulmash, D.; Jacquod, P.; Deshpande, A.; Watanabe, K.; Taniguchi, T.; Jarillo-Herrero, P.; Leroy, B. J. *Nat. Mater.* **2011**, *10*, 282.

8.   Decker, R.; Wang, Y.; Brar, V. W.; Regan, W.; Tsai, H. Z.; Wu, Q.; Gannett, W.; Zettl, A.; Crommie, M. F. *Nano Lett.* **2011**, *11*, 2291.

9.   Schedin, F.; Geim, A. K.; Morozov, S. V.; Hill, E. W.; Blake, P.; Katsnelson, M. I.; Novoselov, K. S. *Nat. Mater.* **2007**, *6*, 652.

10.   Wehling, T. O.; Novoselov, K. S.; Morozov, S. V.; Vdovin, E. E.; Katsnelson, M. I.; Geim, A. K.; Lichtenstein, A. I. *Nano Lett.* **2008**, *8*, 173.

11. Wehling, T. O.; Katsnelson, M. I.; Lichtenstein, A. I. *Chem. Phys. Lett.* **2009**, *476*, 125.

12. Ryu, S.; Liu, L.; Berciaud, S.; Yu, Y. J.; Liu, H. T.; Kim, P.; Flynn, G. W.; Brus, L. E. *Nano Lett.* **2010**, *10*, 4944.

13. Brar, V. W.; Decker, R.; Solowan, H. M.; Wang, Y.; Maserati, L.; Chan, K. T.; Lee, H.; Girit, C. O.; Zettl, A.; Louie, S. G.; Cohen, M. L.; Crommie, M. F. *Nat. Phys.* **2011**, *7*, 43.

14. Wang, X. R.; Li, X. L.; Zhang, L.; Yoon, Y.; Weber, P. K.; Wang, H. L.; Guo, J.; Dai, H. J. *Science* **2009**, *324*, 768.

15. Zhao, L. Y.; He, R.; Rim, K. T.; Schiros, T.; Kim, K. S.; Zhou, H.; Gutierrez, C.; Chockalingam, S. P.; Arguello, C. J.; Palova, L.; Nordlund, D.; Hybertsen, M. S.; Reichman, D. R.; Heinz, T. F.; Kim, P.; Pinczuk, A.; Flynn, G. W.; Pasupathy, A. N. *Science* **2011**, *333*, 999.

16. Xu, K.; Cao, P. G.; Heath, J. R. *Science* **2010**, *329*, 1188.

17. Leenaerts, O.; Partoens, B.; Peeters, F. M. *Phys. Rev. B* **2008**, *77*, 125416.

18. Wehling, T. O.; Lichtenstein, A. I.; Katsnelson, M. I. *Appl. Phys. Lett.* **2008**, *93*, 202110.

19. Cao, P. G.; Xu, K.; Varghese, J. O.; Heath, J. R. *Nano Lett.* **2011**, (ASAP; DOI: 10.1021/nl2036639).

20. Cao, P. G.; Xu, K.; Varghese, J. O.; Heath, J. R. *J. Am. Chem. Soc.* **2011**, *133*, 2334.

21. Stolyarova, E.; Rim, K. T.; Ryu, S. M.; Maultzsch, J.; Kim, P.; Brus, L. E.; Heinz, T. F.; Hybertsen, M. S.; Flynn, G. W. *P. Natl. Acad. Sc.i USA* **2007**, *104*, 9209.

22.   Lui, C. H.; Liu, L.; Mak, K. F.; Flynn, G. W.; Heinz, T. F. *Nature* **2009**, *462*, 339.

23.   Cullen, W. G.; Yamamoto, M.; Burson, K. M.; Chen, J. H.; Jang, C.; Li, L.; Fuhrer, M. S.; Williams, E. D. *Phys. Rev. Lett.* **2010**, *105*, 215504.

24.   Ishigami, M.; Chen, J. H.; Cullen, W. G.; Fuhrer, M. S.; Williams, E. D. *Nano Lett.* **2007**, *7*, 1643.

25.   Zhang, Y. B.; Brar, V. W.; Wang, F.; Girit, C.; Yayon, Y.; Panlasigui, M.; Zettl, A.; Crommie, M. F. *Nat. Phys.* **2008**, *4*, 627.

26.   Xu, K.; Cao, P. G.; Heath, J. R. *Nano Lett.* **2009**, *9*, 4446.

27.   Neto, A. H. C.; Guinea, F.; Peres, N. M. R.; Novoselov, K. S.; Geim, A. K. *Rev. Mod. Phys.* **2009**, *81*, 109.

28.   Gregory, J. K.; Clary, D. C.; Liu, K.; Brown, M. G.; Saykally, R. J. *Science* **1997**, *275*, 814.

29.   Batista, E. R.; Xantheas, S. S.; Jonsson, H. *J. Chem. Phys.* **1998**, *109*, 4546.

30.   Chen, W.; Madhavan, V.; Jamneala, T.; Crommie, M. F. *Phys. Rev. Lett.* **1998**, *80*, 1469.

C h a p t e r   6

Scanning Probe and Photoluminescence Studies of Single-layer Molybdenum Disulfide*

In collaboration with Peter Agbo, Victor Brar, Harry Gray, and James R. Heath
This work has not yet been completed and is still in progress.

6.1 Introduction

Interest in thin films has risen dramatically since the discovery of graphene, with its unique two-dimensional structure and exotic electrical and mechanical properties. Unfortunately, graphene does not possess an intrinsic bandgap, thus rendering it largely inutile for use as a semiconducting material.[1] In contrast, atomically thin molybdenum disulfide and similar layered transition metal chalcogenides exhibit large intrinsic bandgaps. Its sizeable bandgap of about 1.8 eV for single layers and 1.2 eV for bulk makes MoS_2 an attractive material for transistor devices, optoelectronics, and many other applications.[2,3] Unfortunately, many of its properties have not yet been thoroughly characterized, or are poorly understood.

The typical mobility of mechanically exfoliated few-layer (usually 1-3 layers) molybdenum disulfide devices, about 200-500 $cm^2V^{-1}s^{-1}$, is smaller than theoretical values predict or allow.[2–4] The nature of charge transport in MoS_2 itself is currently a matter of debate, with various suggested possibilities for the lowering of mobility values, including phonon scattering, surface defects, Coulomb impurities, and many others.[4,5] Furthermore, CVD-grown MoS_2 devices typically have even lower mobilities – about 5 to 20 $cm^2V^{-1}s^{-1}$ –

than mechanically exfoliated ones.[6,7] The disparity is attributed to grain boundaries, interfacial states, and bandgap tail states, among others.[7]

The properties of two-dimensional materials strongly depend on the substrates on which they rest. The effects of the substrate are two-fold: it directly influences the local electronic structure and topography of the thin film, and traps impurities and adsorbates between itself and the film that further affect the material. Almost every atom can be in contact with the atmosphere or the substrate itself for single-layer 2D materials grown or exfoliated on substrates. It is perhaps best then to consider the 2D material as part of a larger system consisting of the thin film, trapped impurities, and the substrate.

Here we report on the role of trapped impurities, edge states and defects, and the resulting morphology and electronic characteristics of few-layer molybdenum disulfide through scanning probe microscopy techniques. We find that water plays a significant role in altering the structure of the thin films, the local electric field gradient, and the photoluminescence of MoS_2.

6.2 Results and Discussion

Previous work has shown that water is trapped underneath few-layer graphene sheets during mechanical exfoliation, allowing the direct visualization of the adsorbed water trapped between the substrate and the graphene sheet.[8–10] We similarly find that mechanical exfoliation of molybdenum disulfide on different substrates leads to adlayer and droplet-like structures underneath the thin sheets – typically three layers – of MoS_2.

Figures 1a and 1b are representative AFM images showing the adlayers templated by MoS_2 sheets on a muscovite mica (001) surface when exfoliated in air at ambient

conditions (about 42% relative humidity and 22°C). No adlayer structures are found in non-templated regions, consistent with the fact that capillary effects between the probe tip and sample disturb the water layers on bare surfaces. The height of the adlayers on the mica surface was approximately 1 nm – the height of a few adlayers of water. Thus, second and third layers of water can be found on top of the already existing first layer which rests on the mica surface. In contrast with graphene-templated mica, we found that molybdenum disulfide sheets stabilize greater numbers of these multiple adlayers at ambient conditions. These results indicate that the morphology of molybdenum disulfide thin films is distinctly altered and influenced by the substrate and trapped species.

Electrostatic force microscopy (EFM) and Kelvin probe force microscopy (KPFM) can be used to effectively map the electronic structure of a surface. EFM allows one to study the local electric field gradients of a sample, while KPFM can be used to analyze its surface potential. In EFM, a probe tip oscillated near its resonance frequency is raised to a preset height (~10-100 nanometers) above the surface after an initial pass mapping the topography, and the resulting changes in the resonant frequency of the cantilever due to electrostatic forces is recorded while applying a DC voltage. In KPFM, the tip is similarly raised to a preset height after an initial pass to scan the surface topography, but the mechanical oscillation of the tip is switched off. An AC voltage is then applied to the tip, and the cantilever oscillation amplitude at the AC-frequency is measured. If a DC voltage difference exists between the tip and sample, the cantilever will experience an oscillating electric force at the AC-frequency, and this amplitude of oscillation can be used to map the surface potential. Figure 2a shows a schematic of the setup used for measurements. Probing the electronic characteristics of the MoS_2-water-mica system is very interesting and highly

informative because the influence of topographic features on the electronic structure of MoS_2 should be greatly lessened due to the smoothness of the water adlayers on which the MoS_2 sheets rest. Any measured shifts in the electronic spectra should thus be reflective of the influence of the underlying water.

We found that water does indeed perturb the electronic structure of molybdenum disulfide. Figures 1cef are EFM images taken at positive and negative bias along with a KPFM image of the same region. The contrast in the EFM images is reversed when the bias shifts from positive to negative, indicating that the observed images are representative of potential variations.[11] EFM is a largely qualitative technique – it indicates the existence of differences in the local electric field gradient, but can be difficult to interpret since the individual voltage components contributing to the gradient are not separated.[12] KPFM, on the other hand, can yield more quantitative results because it probes the work function of the surface. A contact potential evolved between the tip and surface allows the work function to be directly measured. The KPFM image shows that a potential difference of about 75 mV exists between the water-covered region of MoS_2 and the molybdenum disulfide resting on the bare mica surface. Since the same material – single layer MoS_2 – is being probed, the potential difference is indicative of the change in the Fermi level of the sample. The presence of water raises the Fermi level of MoS_2 with respect to the Fermi level of the material when no water is present. The observed variation is most likely due to the perturbative effects of the dipole moments of water, as was seen in our work with graphene.[13] Local electrostatic fields can be induced by the dipole moments of water and significantly influence the charge carrier density in a material. The influence of electrostatic fields arising from dipoles can be readily seen by examining the dielectric properties of

materials. Even if the total charge in a given substance vanishes, the dielectric polarization vector can still be non-zero. The negative divergence of the dielectric polarization yields the average charge density, and thus determines both the volume charge density and the surface charge density of a material. Using a Gaussian surface to enclose a small element of the surface of a dielectric yields the condition that the surface charge density is then equivalent to the normal component of the dielectric polarization.[14] At very small distances – on the scale of a few Angstroms – the surface charge density plays a very important role in determining the electronic properties of a material. The electric fields associated with these charges can perturb the electronic states of a material by allowing energy to be gained or lost from the field. If the electronic states occupied by the charge carriers are perturbed, the chemical potential or Fermi level will be altered as well.

We also observed a very striking effect due to the trapped water layers on the photoluminescence of single layer molybdenum disulfide. Single layer MoS_2 is a direct bandgap semiconductor that displays a distinct fluorescence peak at 676 nm.[15] When water layers are present under the material – as is the case for MoS_2 exfoliated on mica – the luminescence is quenched and the MoS_2 appears dark. The quenching is perhaps due to a coupling of the hydroxyl group vibrational modes of the underlying water to higher-energy states of the photo-excited electrons for single layer MoS_2. For example, hydroxyl groups have been shown to quench the photoluminescence of Nd-doped laser phosphate glasses, SnO_2:Eu^{3+} nanoparticles, and more.[16,17] The non-radiative energy transfer of electrons in long-lived excited states to the vibrational modes of the OH groups is shown to strongly affect the luminescence of materials. It is very likely that the photo-excited charge carriers in MoS_2 similarly participate in non-radiative decay processes coupled to the vibrational

modes of the underlying water, resulting in the observed quenching of the photoluminescence. These results indicate the importance of proper sample preparation, since the mere presence of trapped water can lead to significantly altered optical properties for single layer MoS_2.

We also exfoliated MoS_2 on another atomically smooth surface – highly oriented pyrolitic graphite (HOPG) – and discovered that the material effectively traps water on this hydrophobic surface as well. Consistent with previous studies, water adsorbs in the form of small droplets found almost ubiquitously at step edges of HOPG or at defects and tears in the surface. Figure 2a displays the trapped nanodroplets with sizes ranging between 5 to 15 nm, and about 30 to 100 nm in diameter. The vertical to horizontal aspect ratio (height to diameter) of the droplets ranges from about 0.05 - 0.5. Small particles appear to be ubiquitously present on the edges of the thicker few-layer MoS_2. They appear to originate at the edges of the MoS_2 layers and are often then moved by the AFM tip over the surface. Even for samples where particles were not observed initially, scanning of the same samples after a few hours, days or more would reveal the formation of these particulates on the edges of the samples. They were found on all the surfaces that we studied. Figures 2b-e are EFM and KPFM images of the same area. Once again, we confirm that we are able to map the potential variations of the surface by observing that the EFM images complement each other upon reversal of the bias voltage polarity. In contrast to the mica surface, adlayers are not stabilized, and so the perturbations of the electronic structure of the molybdenum disulfide are localized to the nanodroplets decorating the step edges and defects of the HOPG. The KPFM images similarly confirm that the water droplets perturb the MoS_2 layers – Figure 2f shows that a 10 mV dip occurs in the surface potential of the material.

Here, the water is seen to affect single layer MoS_2 on HOPG differently from the way it affects single layer MoS_2 on mica. The surface potential is seen to decrease over water nanodroplets, indicating that the Fermi level has decreased in the presence of water. The importance of the substrate in determining the electronic properties of the material is thus clearly illustrated. The influence of the dipole moments of nanodroplets of water is markedly different from the situation observed for adlayers of water. The orientation of the dipoles is evidently dissimilar, and the collective dipole moment of the water molecules is thus certain to be different as evident from analyzing the spatial arrangement of the molecules. We also observe that the particulates are also seen to be at a different potential – about 20 mV lower – than the rest of the MoS_2 surface.

The nanodroplets, in particular, are highly useful in determining the influence of topography on the electronic properties of MoS_2 through EFM. Topography can influence the electric field, since the curvature of the surface is directly proportional to the surface charge density. Small radii of curvature thus increase the local electric field gradient, and nanodroplets with large aspect ratios should cause measurable shifts in the EFM spectra. Our results confirm this, with a typical EFM image showing the influence of these droplets on the electric field gradient in Figure 2b. Moreover, even nanodroplets with smaller aspect ratios demonstrate a shift in the EFM phase, although the step edges of HOPG are not apparent in the EFM image.

Conclusions

Molybdenum disulfide can thus be used to template trapped molecules, demonstrating remarkable conformation to the adsorbed layers and the substrate itself. We

find that water plays a significant role in modifying the morphology, electronic structure, and optical properties of the material. We confirm that the role of the substrate and adsorbed species is perhaps nowhere as important as in a system of two-dimensional materials.

6.4 Experimental Methods

Identification of few layer MoS$_2$

Suitable single and few-layer MoS$_2$ samples were identified by optical microscopy in transmission mode for exfoliated MoS$_2$ on mica. A color contrast was observed in reflection mode optical microscopy for MoS$_2$ on HOPG, with single and few-layers appearing a faint pink-to-purple color. Thicknesses were confirmed by microRaman spectroscopy using a Renishaw M1000 microRaman spectrometer with a 514.5 nm wavelength laser and a 2400 lines per mm grating.

Exfoliation of MoS$_2$ and preparation of mica, HOPG Samples

Molybdenum disulfide was mechanically exfoliated on mica and HOPG under various conditions of relative humidity, and an ambient room temperature of about 22° C. Reduced humidity values of about 4 to 5% were achieved by exfoliating MoS$_2$ in a glovebox which was continually purged with high-purity nitrogen. The Scotch tape used for exfoliation was prepared inside the glovebox, as well as the substrates for different humidity conditions. Both mica discs (1 cm diameter muscovite, Ted Pella) and HOPG (Grade ZYB, 2SPI) were cleaved and allowed to equilibrate for 15 minutes before exfoliation.
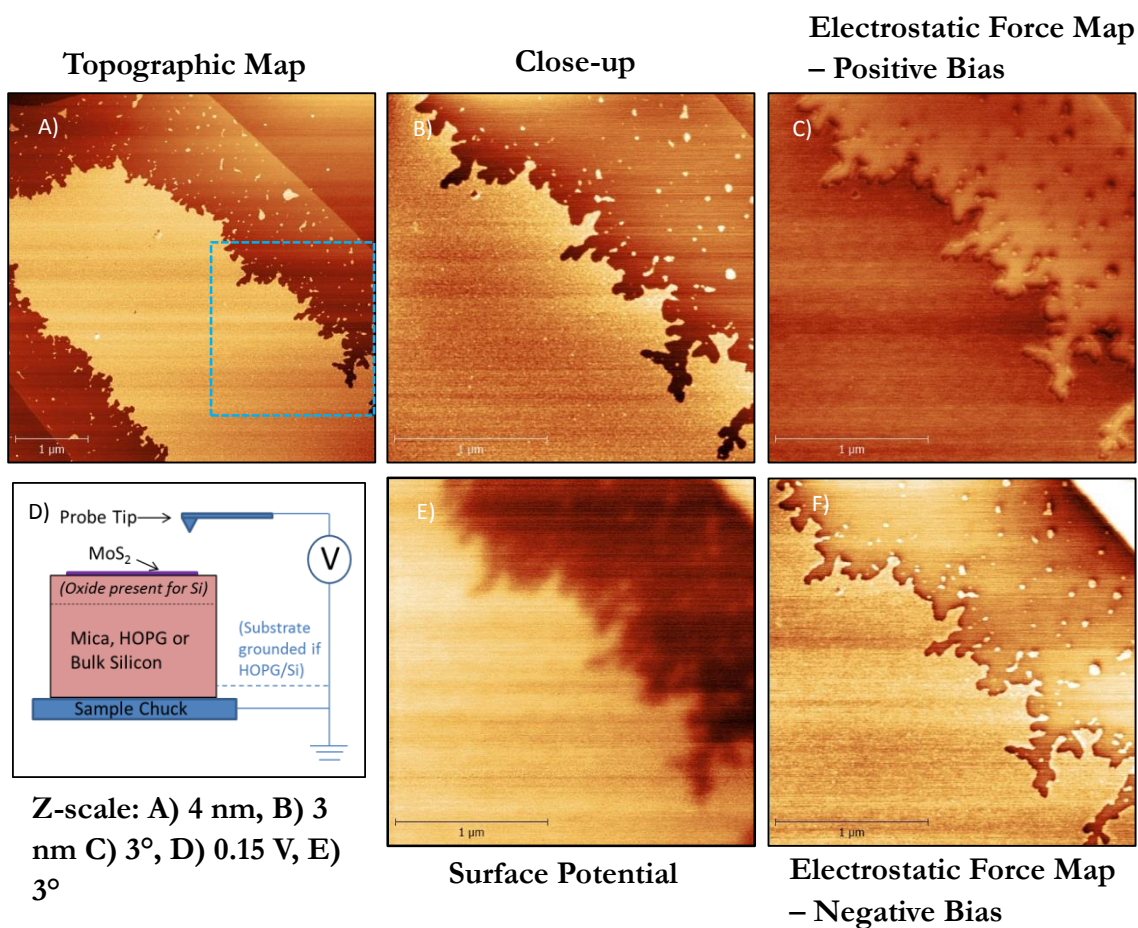
AFM, EFM & KPFM

AFM, EFM & KPFM characterizations were performed at ambient conditions using a Digital Instruments Nanoscope IIIa in Tapping Mode. Bruker TESP tips were used with a typical resonance frequency of 320 kHz, tip radius of 8 nm, and force constant of 42 N/m. Calibration was performed on grade ZYB freshly cleaved HOPG surfaces purchased from 2SPI.

Photoluminescence

Fluorescence images were obtained using an Olympus IX81 microscope with a 40x objective and a Cy5 mirror cube. The mirror cube uses a dichroic mirror with cut-on wavelength at 660 nm, an excitation bandpass filter centered at a wavelength of 624 nm with 40 nm bandwidth, and an emission bandpass filter centered at a wavelength of 692 nm with 40 nm bandwidth.

6.5 Figures

Topographic Map **Close-up** **Electrostatic Force Map – Positive Bias**

Z-scale: A) 4 nm, B) 3 nm C) 3°, D) 0.15 V, E) 3°

Surface Potential **Electrostatic Force Map – Negative Bias**

Figure 1- AFM, EFM, and KPFM images of MoS$_2$ on mica

Topographic Map

Electrostatic Force Map – Positive Bias

Electrostatic Force Map – Negative Bias

Surface Potential Map

Z-scale: A) 10 nm, B) 2°, C) 2°, D) 0.20 V, E) 0.10 V
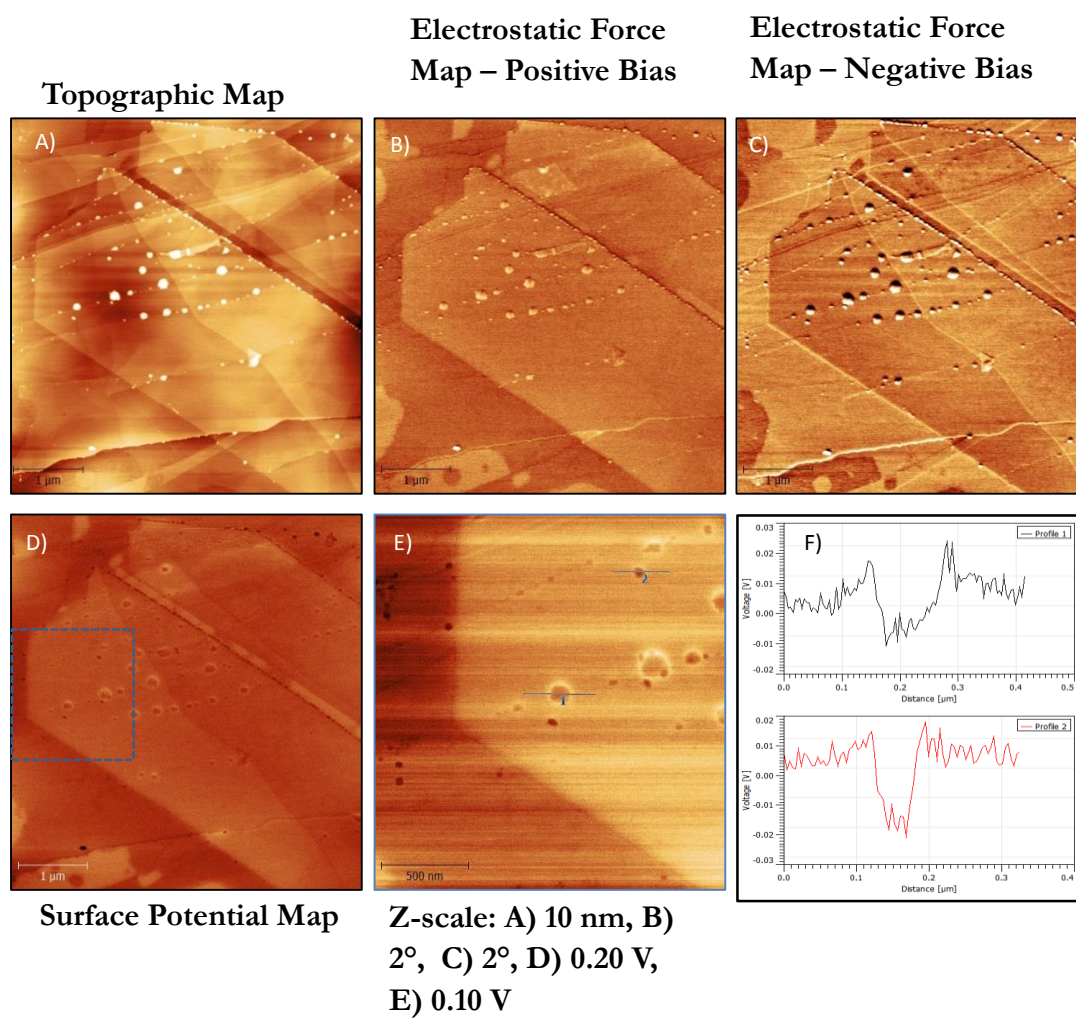
Figure 2- AFM, EFM, and KPFM images of MoS_2 on HOPG

Single-layer MoS$_2$

Water-covered regions appears dark

MoS$_2$
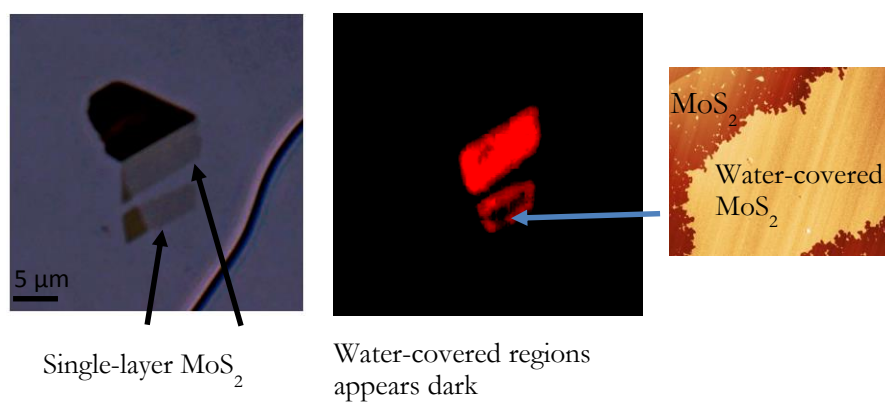
Water-covered MoS$_2$

5 μm

Figure 3 – Photoluminescence of single layer MoS$_2$ on Mica

6.6 References

(1) Loh, K. P.; Bao, Q.; Ang, P. K.; Yang, J. *J. Mater. Chem.* **2010**, *20*, 2277–2289.

(2) Zhu, W.; Low, T.; Lee, Y.-H.; Wang, H.; Farmer, D. B.; Kong, J.; Xia, F.; Avouris, P. *Nat. Commun.* **2014**, *5*.

(3) Qiu, H.; Xu, T.; Wang, Z.; Ren, W.; Nan, H.; Ni, Z.; Chen, Q.; Yuan, S.; Miao, F.; Song, F.; Long, G.; Shi, Y.; Sun, L.; Wang, J.; Wang, X. *Nat. Commun.* **2013**, *4*.

(4) Radisavljevic, B.; Radenovic, A.; Brivio, J.; Giacometti, V.; Kis, A. *Nat. Nanotechnol.* **2011**, *6*, 147–150.

(5) Kaasbjerg, K.; Thygesen, K. S.; Jacobsen, K. W. *Phys. Rev. B* **2012**, *85*, 115317.

(6) Liu, H.; Si, M.; Najmaei, S.; Neal, A. T.; Du, Y.; Ajayan, P. M.; Lou, J.; Ye, P. D. *Nano Lett.* **2013**, *13*, 2640–2646.

(7) Amani, M.; Chin, M. L.; Birdwell, A. G.; O'Regan, T. P.; Najmaei, S.; Liu, Z.; Ajayan, P. M.; Lou, J.; Dubey, M. *Appl. Phys. Lett.* **2013**, *102*, 193107.

(8) Xu, K.; Cao, P.; Heath, J. R. *Science* **2010**, *329*, 1188–1191.

(9) Cao, P.; Xu, K.; Varghese, J. O.; Heath, J. R. *Nano Lett.* **2011**, *11*, 5581–5586.

(10) Cao, P.; Xu, K.; Varghese, J. O.; Heath, J. R. *J. Am. Chem. Soc.* **2011**, *133*, 2334–2337.

(11) Lu, Y.; Muñoz, M.; Steplecaru, C. S.; Hao, C.; Bai, M.; Garcia, N.; Schindler, K.; Esquinazi, P. *Phys. Rev. Lett.* **2006**, *97*, 076805.

(12) Panchal, V.; Pearce, R.; Yakimova, R.; Tzalenchuk, A.; Kazakova, O. *Sci. Rep.* **2013**, *3*.

(13) Cao, P.; Varghese, J. O.; Xu, K.; Heath, J. R. *Nano Lett.* **2012**, *12*, 1459–1463.

(14) In *Electrodynamics of Continuous Media (Second Edition revised and enlarged)*; LANDAU, L. D.; LIFSHITZ, E. M., Eds.; Course of Theoretical Physics; Pergamon: Amsterdam, 1984; Vol. 8, p. 34.

(15) Yin, Z.; Li, H.; Li, H.; Jiang, L.; Shi, Y.; Sun, Y.; Lu, G.; Zhang, Q.; Chen, X.; Zhang, H. *ACS Nano* **2012**, *6*, 74–80.

(16) Ehrmann, P. R.; Carlson, K.; Campbell, J. H.; Click, C. A.; Brow, R. K. *J. Non-Cryst. Solids* **2004**, *349*, 105–114.

(17) Moon, T.; Hwang, S.-T.; Jung, D.-R.; Son, D.; Kim, C.; Kim, J.; Kang, M.; Park, B. *J. Phys. Chem. C* **2007**, *111*, 4164–4167.

C h a p t e r 7

Activation and Degradation of Akt in Live Cells*

In collaboration with Ryan Henning, Samir Das, Arundhati Nag, Grace Tang, Kevin Tang, and James R. Heath.
This work has not yet been completed and is still in progress.

7.1 Introduction

Perturbing protein function has been a valuable method for elucidating protein signal transduction pathways.[1] Perturbations can include inhibition, activation, and removal of a protein of interest. Inhibition is commonly achieved with small molecules or genetic manipulation resulting in an inactive protein. Activation can be achieved similarly with genetic amplification or with small molecules. Additionally, proteins can be selectively removed from cells via genetic knockdown, siRNA, and more recently by using proteolysis targeting chimeric molecules, or protacs.[2] Here we report on the use of protein catalyzed capture agents to induce all three perturbations to the serine/threonine protein kinase AKT and demonstrate in-cell activation, inhibition, and degradation of AKT.

Efficient binding of the Akt2 protein from cell lysate has been previously demonstrated using protein capture agents. These multiligand synthetic peptides display high affinity and selectivity toward their desired targets, and are far more robust than their antibody counterparts. We previously reported on the development and characterization of two such capture agents, where their efficacy in pulling down Akt2 protein from cell lysate was analyzed.[3] They were also seen to activate and inhibit Akt2 enzymatic activity in *in vitro* kinase assays. The synthetic approach to their development uniquely enables one to functionalize them with various moieties. We have since been able to directly bind proteins

in live cells using capture agents bound to cell penetrating peptides (CPPs). Several

studies have shown that CPPs efficiently penetrate cell membranes and are frequently used

to allow CPP-bound molecules to enter cells.[4] To exploit this ability we covalently bound

HIV TAT, a CPP that is particularly effective at traversing the cell membrane, to our

capture agents and studied their effects on live cells. We also functionalized the capture

agents with other moieties and analyzed their effects on the biology of the cells. We show

that we are able to induce activation of the targeted protein pathway, and degradation of the

Akt protein *in vivo*.

7.2 Experimental Methods

Solid phase peptide synthesis:

General protocol: Peptides were synthesized on Rink Amide MBHA, Biotin Novatag, and

Sieber Amide resin either manually or on a Titan 357 Automatic Peptide Synthesizer

(AAPPTec). Peptide coupling reactions were done in NMP with 2 equivalents of amino

acid, 2 equivalents of HATU, and 6 equivalents of N,N-Diisopropylethylamine (Sigma).

For removal of Nα-Fmoc protecting groups, a solution of 20% piperidine in NMP was

used.

Acylation: The resin was treated twice for 10 minutes with a solution of anhydrous acetic

anhydride and DIEA in NMP (acetic anhydride: DIEA: Peptide; 40:20:1) at room

temperature. Excess reagent was removed by washing 5 times successively with NMP.

Cleavage of side chain protected peptides: The peptides were synthesized on Sieber Amide resin and cleaved by washing 3 times for one minute with 1% TFA/DCM, and finally washed with DCM. The acidic peptide solution was neutralized using 2 equivalents of DIEA, followed by removal of the solvent by rotary evaporation. The remaining semisolid was dissolved in filtered DMSO, HPLC grade acetonitrile and double distilled water, and purified via HPLC.

Cleavage of side chain deprotected Biotin Linker peptide: The peptides were synthesized on Biotin Novatag resin. The dried resin was then treated with a TFA cleavage solution of 95% TFA, 2.5% H_2O, and 2.5% triethylsilane for 2 hours at room temperature. The cleavage solution was filtered to remove the resin and added dropwise to an ice-cooled solution of diethyl ether.

Cleavage of TAT-containing peptides: TAT-containing peptides were synthesized on Rink Amide MBHA resin. The dried resin was then incubated with a TFA cleavage solution of 80% TFA, 10% thioanisole, 5% H_2O, 5% triethylsilane for 3 hours at room temperature. The cleavage solution was filtered to remove the resin and added dropwise to an ice-cooled solution of diethyl ether.

HPLC purification of peptides: All peptides were purified using a preparative or semi-preparative scale HPLC with a C18 reverse phase column. A gradient of double distilled water and HPLC grade acetonitrile and 0.1% TFA was used for all purifications.

Protocol for on-bead copper (Cu) catalyzed azide alkyne cycloaddition (CuAAC) click reaction: On-bead Cu catalyzed click reactions were performed with the azide on bead and the alkyne in solution. The resin was treated with 2 equivalents of the relevant alkyne, 1.5 equivalents of CuI (Sigma) and 2.5 equivalents of ascorbic acid (Sigma), in a solution of 20% piperidine in DMF. The reaction was performed overnight at room temperature. Excess copper was removed from the resin by washing with a Cu chelating solution (5% (w/v) sodium diethyl dithiocarbamate, 5% (v/v) DIEA in DMF).

Removal of Dde protecting group: For removal of Dde protecting groups, resin-bound peptide was washed with a solution of 2% hydrazine in DMF 3 times for 10 minutes.

Biological Assays and Microscopy:

Cell culture: All cell lines were purchased from American Type Culture collection and cultured under conditions specified by the provider.

Immunoblotting: Western blots were performed according to standard protocols. Briefly, cells were lysed with cell lysis buffer (Cell Signaling Technology) containing protease and phosphatase inhibitors (Cell Signaling Technology). Cell lysates were quantified with a Bradford protein assay (Thermo Scientific) and prepared for gel electrophoresis in Laemmli sample buffer and reducing agent. 20 µg of cell lysate were added to precast polyacrylamide gels (Bio-Rad) and proteins were separated by electrophoresis followed by transfer to PVDF membrane. Membranes were then blocked and probed with primary antibodies followed by horseradish peroxidase-conjugated secondary antibodies. The

following antibodies were used according to manufacturer protcol: p-GSK3β (Cell

Signaling, 9323), GSK3 β (Cell Signaling, 12456), AKT (Cell Signaling, 4691), p-AKT

(S473) (Cell Signaling, 4060), Actin (Cell Signaling, 8456), and HRP-linked Anti-rabbit

IgG (Cell Signaling, 7074). The bands were visualized by chemiluminescence (Thermo

Scientific).

XTT assay: The XTT assay kit was purchased from Cell Signaling Technology (#9095)

and used according to manufacturer protocol. Briefly, $1x10^4$ cells were seeded in a 96-well

plate. The following day, cells were serum starved and treated with capture agent.

Following treatment, the XTT tetrazolium salt was added to the media, and after 1 hour the

absorbance at 450 nm was measured in a 96-well plate reader.

In-cell ELISA assay: In-cell ELISA kits were purchased from Thermo Scientific (#62215)

and used according to manufacturer protocol. Briefly, $1x10^4$ cells were seeded in 384-well

plates and allowed to attach overnight. The following day, cells were serum starved and

treated with capture agent. Following capture agent treatment, cells were fixed,

permeablized, blocked, and then stained with primary and HRP-conjugated secondary

antibody and developed with colorimetric peroxidase substrate. The absorbance was

measured at 450 nm to quantify the protein.

Fluorescence microscopy: Cells were seeded onto chambered coverglass slides (Sigma)

and allowed to attach overnight. The following day, cells were serum starved and treated

with fluorescent capture agent. Live cells were then imaged using a Zeiss LSM 5
Exciter microscope.

7.3 Results and Discussion

The structure of the TAT-bound N-terminal capture agent is shown in Figure 1,
where the HIV TAT sequence is separated from the capture agent by two PEG spacers and
a protected-lysine residue that could be further functionalized as desired (adding a dye,
etc.). To validate cellular uptake, we treated U87 cells with fluorescently labeled capture
agent and acquired simultaneous fluorescence and transmission images. U87 cells are
particularly useful for imaging since they grow in a uniform monolayer. We found that the
molecule is able to efficiently penetrate the cell membrane and enter the cells. No
fluorescence signals were detected in the regions outside the cells.

Once we had confirmed that the TAT-bound capture agent was indeed entering
cells, we performed cellular assays targeting the Ak2 protein pathway. Akt2 phosphorylates
GSK-3β, and thus its enzymatic activity can be monitored by studying its effects on this
particular protein.[5] Ovarian cancer cells from the SKOV3 cell line were treated with the
TAT-coupled activating triligand for various intervals of time and then simultaneously
lysed. Untreated cells as well as EGF-stimulated cells were also used as a control. The level
of p-GSK-3β was seen to increase after 1 hour of treatment, decrease over the next few
hours, and finally increase once more – perhaps alluding to a feedback mechanism in the
cell. The 1-hour treatment point shows a clear increase in the p-GSK-3β level relative to
both the untreated and EGF-stimulated cells. On the other hand, the p-Akt level
monotonically decreases over the entire time course. This indicates that the activity of

capture agent bound-Akt is independent of its phosphorylation and activation at the S473 site. Thus, the N-terminal capture agent is able to significantly activate the Akt protein even in the absence of cellular phosphorylation.

We also performed cell viability assays using XTT-tetrazolium salt. Dehydrogenase enzymes in live cells reduce XTT to a vividly colored formazan dye that can be used to quantify the number of viable cells. We found that the NP1 triligand has a dramatic effect on both OVCAR3 and SKOV3 cell lines. We see a sharp increase in the cell number, followed by a gradually sloping decrease, perhaps indicating the presence of a feedback loop in the cellular metabolic pathways.

In addition to controlling Akt enzymatic activity with PCC agents, chemical functionality can be encoded into these molecules. Thus far we have incorporated a biotin affinity handle, fluorescent labels for imaging, and the HIV-TAT peptide for cellular delivery. Sequence specific cellular signals can also be incorporated to elicit desired biological effects. Cells utilize chemical signals to catalyze myriad effects that are necessary for life. One such example of using cellular signals to control proteins is the recent development of proteolysis targeting chimeric molecules, or protacs.[6] Protacs utilize the cell's quality-control machinery by artificially targeting proteins for proteasomal degradation. We sought to turn the N and C-terminal triligands into protacs by encoding a peptide ligand for the E3 ubiquitin ligase von Hippel Lindau protein, VHL. Figures 6 and 7 show the structure of the N and C-terminal triligands with the VHL binding site from Hypoxia Inducible Factor 1α protein. We hypothesized that capture agent-induced recruitment of VHL to Akt could result in ubiquitination and proteasomal degradation of Akt.

Upon treatment of OVCAR3 cells with the capture agents-protacs there is a rapid decrease in total Akt per cell, with the minimum levels reached by 4 hours. We also observed a dose-dependent decrease in Akt per cell beginning with a 25 μM final concentration of the N-terminal protac. Both N- and C-terminal protacs were able to induce Akt degradation.

7.4 Conclusions

We have demonstrated both activation and degradation of Akt in live cells using synthetic peptides. The synthetic approach allows one to directly encode molecules with functionality as desired. This provides a route by which to effect biological changes or perturbations in a specific and controlled manner. An example of this concept is demonstrated by directly degrading the Akt protein in vivo.

7.5 Figures
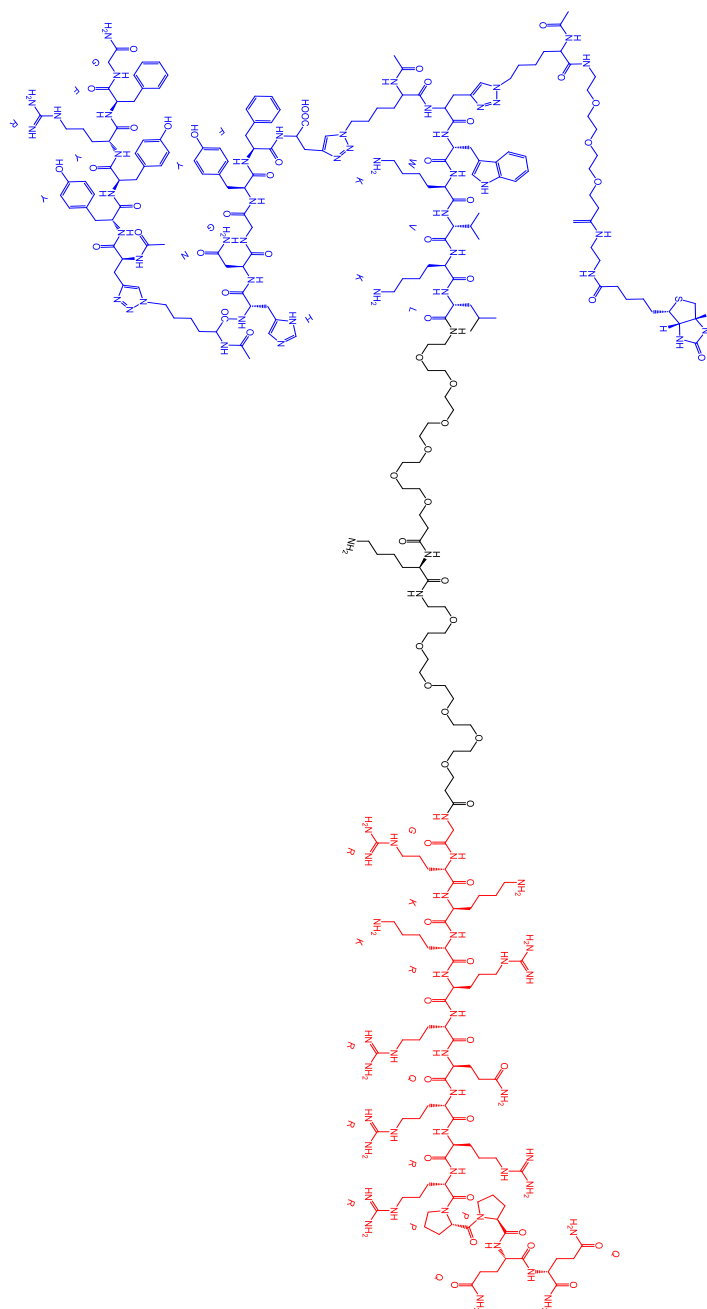
Figure 1 – N-terminal Activator. The N-terminal capture agent (blue) is separated from the TAT sequence (red), by two PEG spacers and a lysine residue that can be further functionalized.
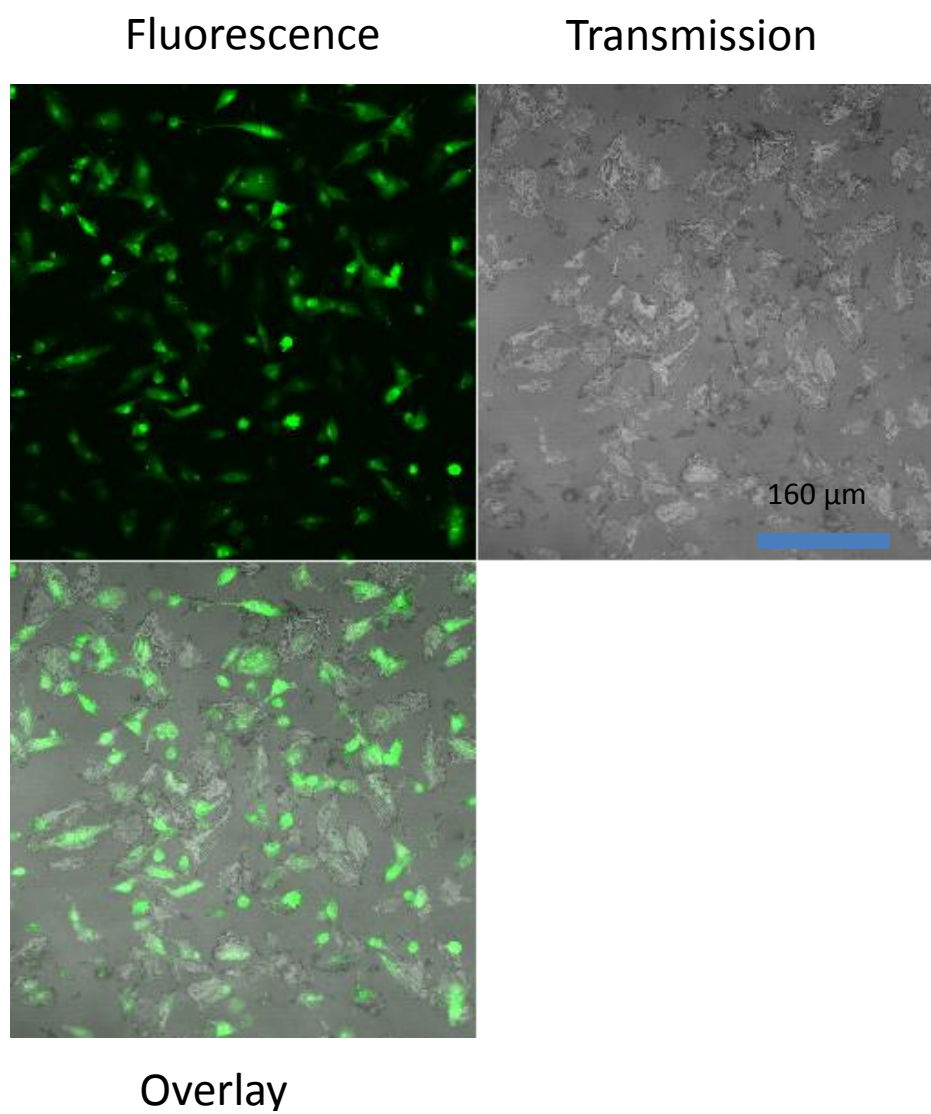
Fluorescence   Transmission

160 µm

Overlay

Figure 2 – Optical images of U87 cells treated with N-terminal activator. Fluorescence, transmission, and an overlay of the two are depicted.
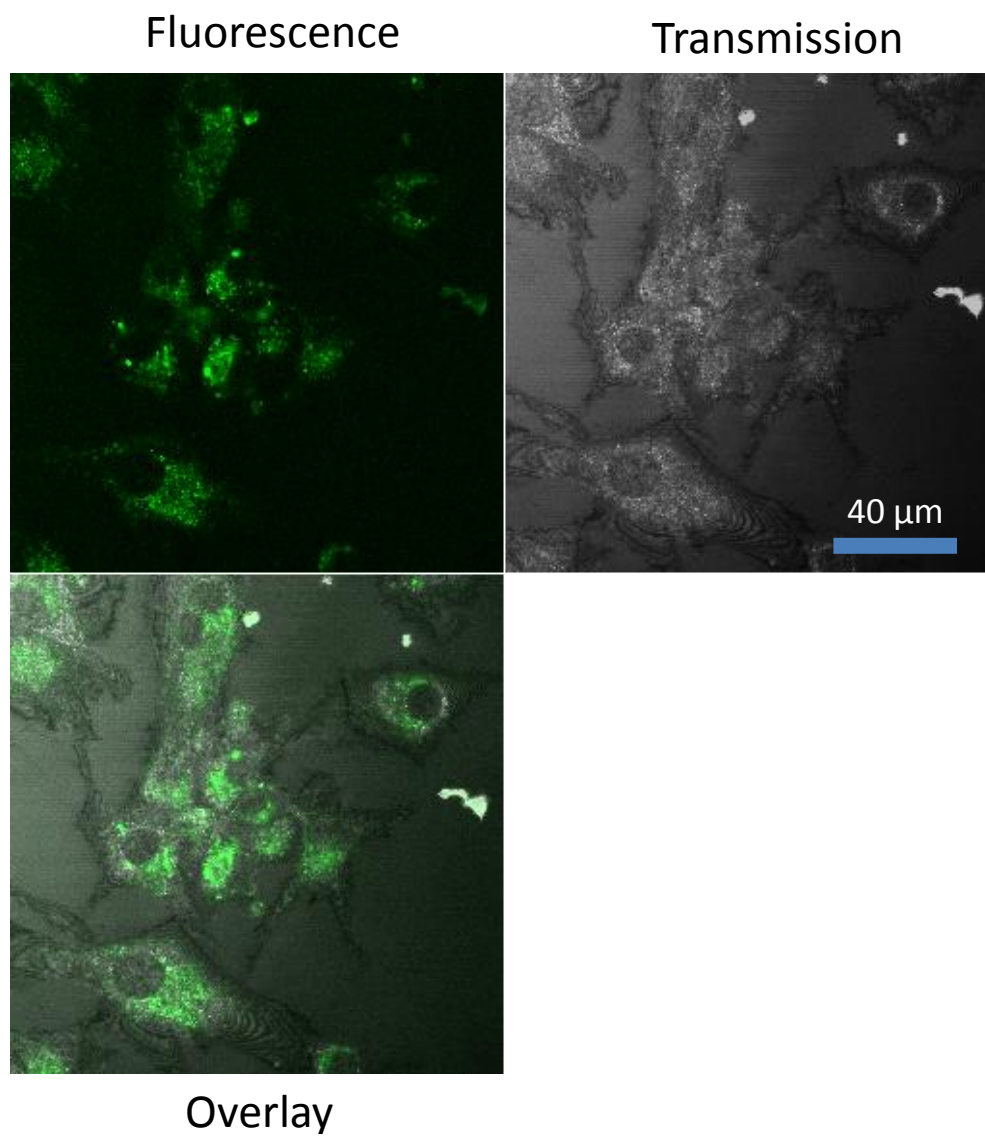
Fluorescence

Transmission

40 µm

Overlay

Figure 3 – Close-up optical images of U87 cells treated with N-terminal activator. The higher magnification allows one to see cellular features such as the nuclei of the cells.
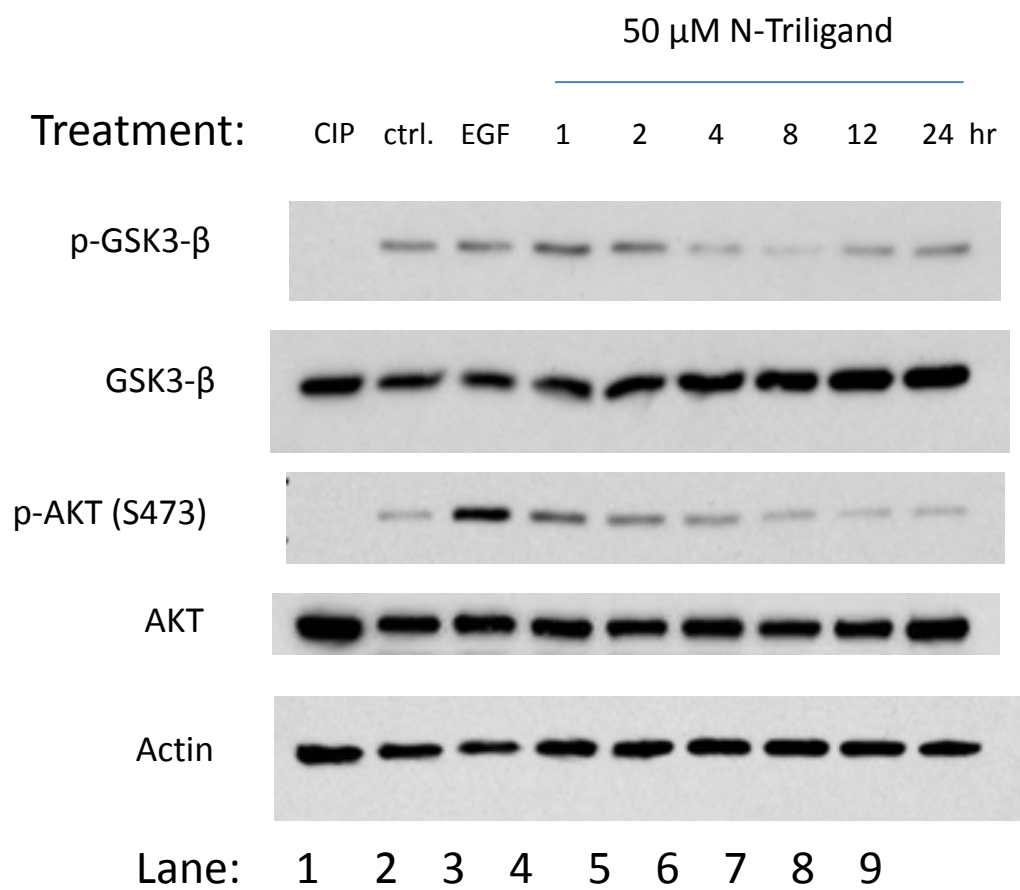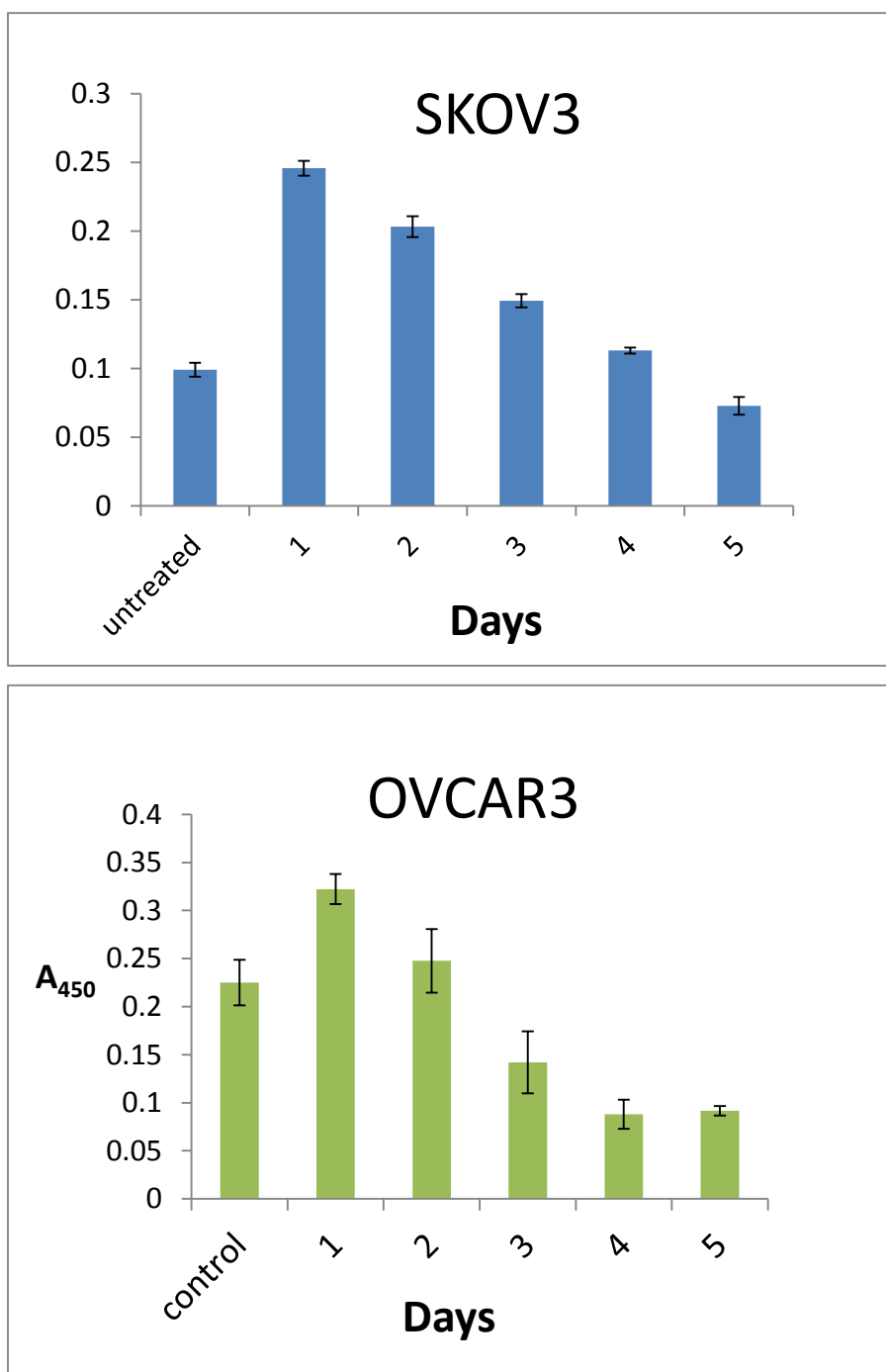
Figure 4 – Western blot of SKOV3 cells treated with N-terminal activator.

Figure 5 – XTT assays of SKOV3 and OVCAR3 cells treated with N-terminal activator.
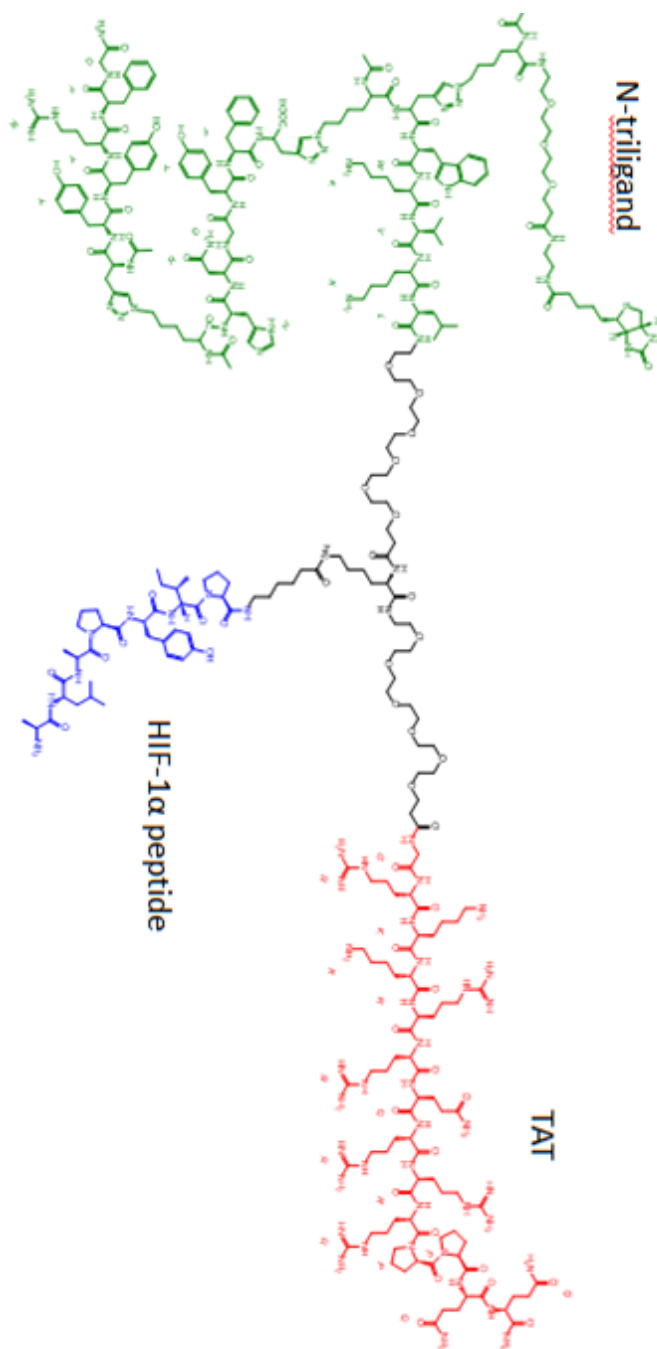
Figure 6 – N-terminal activator functionalized with degradation signal.
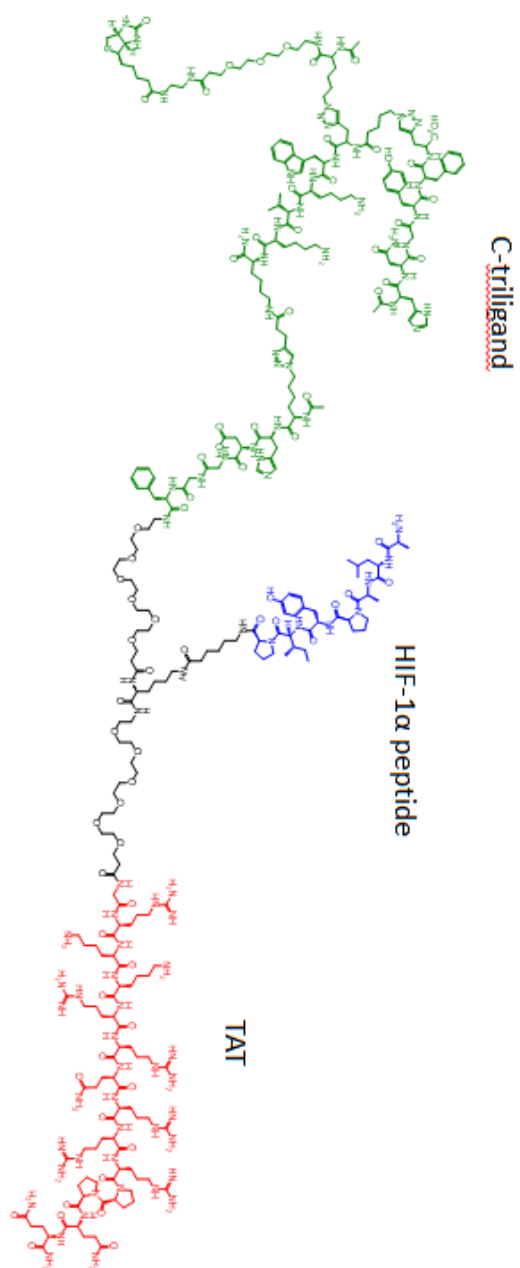
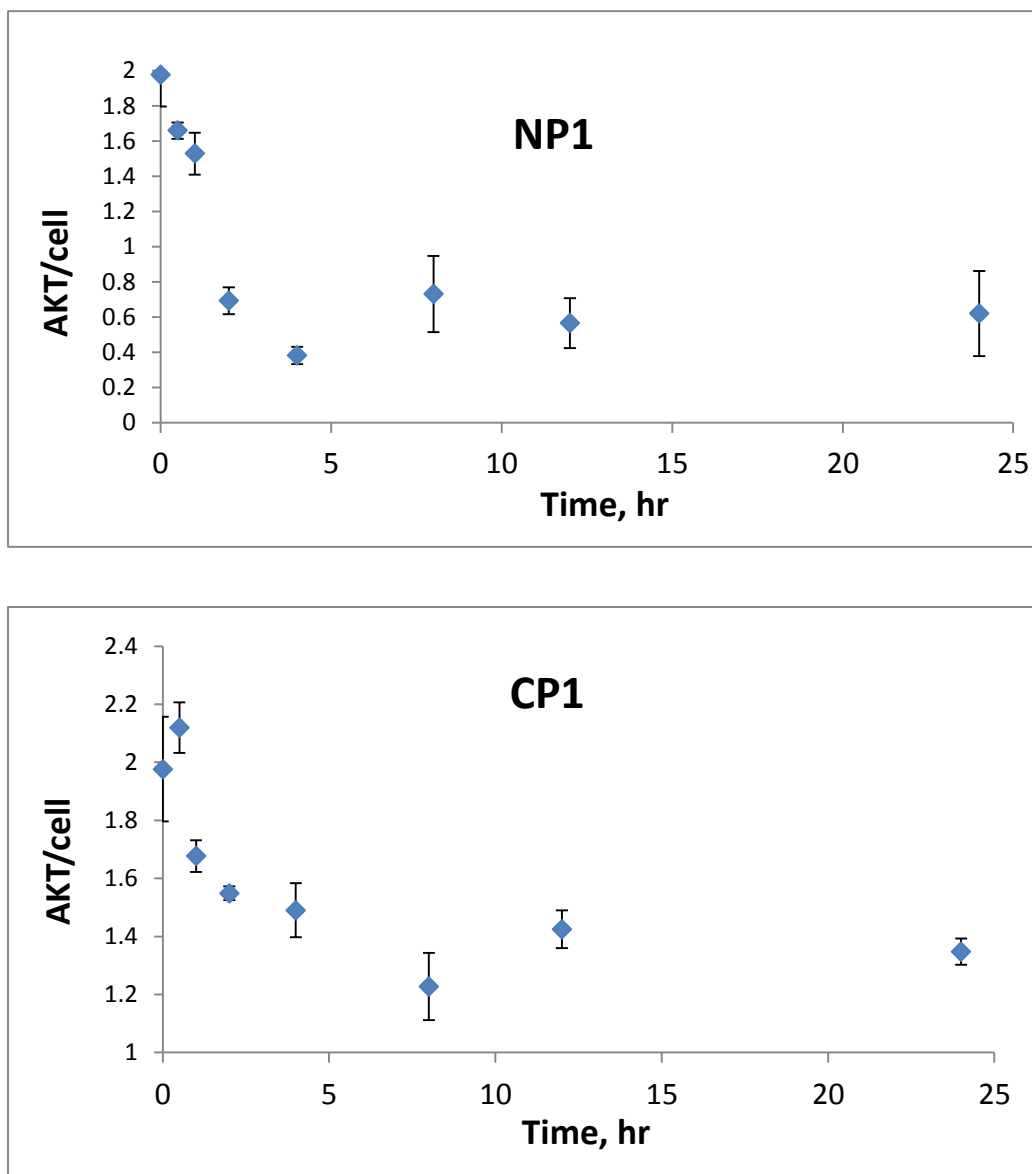Figure 7 – C-terminal inhibitor functionalized with degradation signal.

Figure 8 – ELISAs of treatment of OVCAR3 cells with degradation signal on both N-terminal and C-terminal capture agents

7.6 References

1.	Alaimo, P. J., Shogren-Knaak, M. A. & Shokat, K. M. Chemical genetic approaches for the elucidation of signaling pathways. *Curr. Opin. Chem. Biol.* **5,** 360–367 (2001).

2.	Buckley, D. L. & Crews, C. M. Small-Molecule Control of Intracellular Protein Levels through Modulation of the Ubiquitin Proteasome System. *Angew. Chem. Int. Ed.* **53,** 2312–2330 (2014).

3.	Nag, A. *et al.* A Chemical Epitope-Targeting Strategy for Protein Capture Agents: The Serine 474 Epitope of the Kinase Akt2. *Angew. Chem. Int. Ed.* **52,** 13975–13979 (2013).

4.	Heitz, F., Morris, M. C. & Divita, G. Twenty years of cell-penetrating peptides: from molecular mechanisms to therapeutics. *Br. J. Pharmacol.* **157,** 195–206 (2009).

5.	Engelman, J. A. Targeting PI3K signalling in cancer: opportunities, challenges and limitations. *Nat. Rev. Cancer* **9,** 550–562 (2009).

6.	Hines, J., Gough, J. D., Corson, T. W. & Crews, C. M. Posttranslational protein knockdown coupled to receptor tyrosine kinase activation with phosphoPROTACs. *Proc. Natl. Acad. Sci.* **110,** 8942–8947 (2013).

7.	Sakamoto, K. M. *et al.* Protacs: Chimeric molecules that target proteins to the Skp1–Cullin–F box complex for ubiquitination and degradation. *Proc. Natl. Acad. Sci.* **98,** 8554–8559 (2001).

8.   Tae, H. S. *et al.* Identification of Hydrophobic Tags for the Degradation of Stabilized Proteins. *ChemBioChem* **13,** 538–541 (2012).

9.   Long, M. J. C., Gollapalli, D. R. & Hedstrom, L. Inhibitor Mediated Protein Degradation. *Chem. Biol.* **19,** 629–637 (2012).